



저작자표시-비영리-변경금지 2.0 대한민국

이용자는 아래의 조건을 따르는 경우에 한하여 자유롭게

- 이 저작물을 복제, 배포, 전송, 전시, 공연 및 방송할 수 있습니다.

다음과 같은 조건을 따라야 합니다:



저작자표시. 귀하는 원저작자를 표시하여야 합니다.



비영리. 귀하는 이 저작물을 영리 목적으로 이용할 수 없습니다.



변경금지. 귀하는 이 저작물을 개작, 변형 또는 가공할 수 없습니다.

- 귀하는, 이 저작물의 재이용이나 배포의 경우, 이 저작물에 적용된 이용허락조건을 명확하게 나타내어야 합니다.
- 저작권자로부터 별도의 허가를 받으면 이러한 조건들은 적용되지 않습니다.

저작권법에 따른 이용자의 권리는 위의 내용에 의하여 영향을 받지 않습니다.

이것은 [이용허락규약\(Legal Code\)](#)을 이해하기 쉽게 요약한 것입니다.

[Disclaimer](#)

공학석사 학위논문

Evaluation of formability on
complex concentrated alloys with
different deformation mechanism

변형 기구에 따른 콤플렉스 고용 합금의
성형성 평가

2020 년 2 월

서울대학교 대학원
재료공학부
예 정 원

Abstract

Evaluation of formability on complex concentrated alloys with different deformation mechanism

Jeong Won Yeh

Department of Materials Science and Engineering

College of Engineering

Seoul National University

The rapid evolution of modern industries demands advanced materials exhibiting greatly improved performances. Recently, the development strategies of complex concentrated alloys (CCAs) have shown great potential to resolve these challenges with their inherent mechanisms of damage tolerance under extreme environments such as high stress, high temperature and high radiation flux. However, in order to commercialize CCAs, the formability enhancement should be considered because the ability is closely related to plastically deform without being damaged. However, there is very little attention up to date to evaluate formability in these materials. Herein, we systematically demonstrate the effect of deformation mechanism on the formability in FCC HEAs. Therefore, CCAs with different deformation mechanisms such as dislocation gliding (Slip), twinning induced plasticity (TWIP), and transformation induced plasticity (TRIP and TaDP) were prepared by controlling the stacking fault energy (SFE) of the material through

thermodynamic calculation. As a results, the Forming Limit Diagram and limit dome height test of FCC HEAs with different deformation mechanisms are carefully constructed by numerical simulations and experiments, respectively. Through this, it was found that in the case of TRIP and TaDP CCAs having phase transformation-based deformation mechanism, the formability was reduced compared to uniform elongation under uniaxial stress state. In order to understand this phenomenon, we tried to analyze the evolution of microstructure under various stress state. Indeed, this result would offer an essential guideline how to design HEAs with optimal shape as well as properties for harsh environments.

Keywords: complex concentrated alloys (CCAs), deformation mechanism, forming limit diagram (FLD), limit dome height test (LDH), stress state analysis

Student number: 2018-25610

Table of Contents

| | |
|---|------------|
| Abstract..... | i |
| Table of Contents | iii |
| List of Figures | vii |
| List of Tables | xii |
| | |
| Chapter 1. Introduction..... | 1 |
| 1.1. Concept of complex concentrated alloys..... | 1 |
| 1.1.1. Definition and characteristics | 1 |
| 1.1.2. Four core effects of complex concentrated alloys | 3 |
| 1.2. Necessity of evaluating formability | 9 |
| 1.3. Measurement of formability | 14 |
| 1.3.1. Forming limit diagram | 16 |
| 1.3.2. Limit dome height test..... | 20 |
| 1.4. Stress state analysis | 22 |
| 1.4.1. Concept of triaxiality..... | 22 |
| 1.4.2. Fracture test..... | 26 |
| 1.5. Motivation and scope | 28 |

| | |
|---|-----------|
| Chapter 2. Experimental procedure..... | 30 |
| 2.1. Sample preparation..... | 30 |
| 2.1.1. Casting procedure..... | 30 |
| 2.1.2. Post processing..... | 32 |
| 2.2. Microstructural characterization..... | 34 |
| 2.3. Mechanical analysis | 36 |
| 2.3.1. Uniaxial tensile test..... | 36 |
| 2.3.2. Limit dome height test..... | 39 |
| 2.4. Calculation method of forming limit diagram..... | 41 |
| 2.5. Simulation method of stress state analysis | 43 |

Chapter 3. Formability of complex concentrated alloys with different deformation mechanism..... 46

| | |
|--|----|
| 3.1. Deformation mechanism difference depending on stacking faults energy..... | 46 |
| 3.2. Microstructure prior to the deformation | 48 |
| 3.3. Uniaxial tensile test..... | 52 |
| 3.3.1. Uniaxial tensile test depending on rolling direction | 52 |
| 3.3.2. Anisotropy factor (R-value) | 59 |
| 3.4. Forming limit diagram prediction | 61 |
| 3.4.1 Hardening law (Swift, Voce) | 61 |
| 3.4.2 Yield criteria (Mises, Hill 48, Yld 2000)..... | 64 |
| 3.4.3 FLD prediction based on M-K model | 67 |

| | | |
|------|---|----|
| 3.5. | Limit dome height test..... | 71 |
| 3.6. | Trade-off between uniaxial stress state and biaxial stress state..... | 75 |

Chapter 4. Effect of stress state on formability 77

| | | |
|--------|---|----|
| 4.1. | Effect of stress state on deformation behavior of TWIP complex concentrated alloy | 80 |
| 4.1.1. | Equivalent strain and stress history | 80 |
| 4.1.2. | Comparison of twinning thickness under different stress states by using ECCI analysis | 82 |
| 4.2. | Effect of stress state on deformation behavior of TRIP complex concentrated alloy | 86 |
| 4.2.1. | Equivalent strain and stress history | 86 |
| 4.2.2. | Comparison of phase transformation under different stress states by using EBSD analysis | 88 |
| 4.3. | Effect of stress state on deformation behavior of TaDP complex concentrated alloy | 92 |
| 4.3.1. | Equivalent strain and stress history | 92 |
| 4.3.2. | Comparison of phase transformation under different stress states by using EBSD analysis | 94 |
| 4.4. | Comparison of deformation behavior under various stress state..... | 98 |

Chapter 5. Conclusions 100

| | |
|---------------------------------|------------|
| Bibliography | I |
| Abstract in Korean | VII |
| Acknowledgements | IX |

List of Figures

Figure 1.1. Schematic diagram for alloy design of multicomponent system. Reused from [1] with permission through “Copyright Clearance Center”.

Figure 1.2. Illustration of ΔS_{mix} for ternary alloy system. Reused from [14] with permission through “Copyright Clearance Center” .

Figure 1.3. Schematic view of severe lattice distortion effects on Bragg diffraction. (A) Perfect lattice with pure alloy. (B) Distorted lattice with multi principal elements. (C) Influence of temperature and distortion effects on the XRD intensity. Reused from [15] with permission through “Copyright Clearance Center” .

Figure 1.4. Schematic illustration of the difference of fluctuation of lattice potential energy during the migration of Ni atom in different matrices. Reused from [16] with permission through “Copyright Clearance Center” .

Figure 1.5. (A) Example of commercial alloys used in the automotive industry. Reused from [22] with permission through “Copyright Clearance Center”. (B) Overview of forming limit curves for different commercial steel. Reused from [18] with permission through “Copyright Clearance Center”.

Figure 1.6. Mechanical properties of TWIP 940 steel. (A) Variation of the strain rate sensitivity value (m value) of TWIP 940 steel with respect to strain and strain rate. Reused from [19] with permission through “Copyright Clearance Center”. (B) Magnified dynamic strain aging section of tensile curve. Reused from [19] with permission through “Copyright Clearance Center”.

Figure 1.7. Schematic of several major/minor combinations in forming limit diagram [27].

Figure 1.8. Experimental determination of the forming limit diagram. (A)

Schematic of sample dimension used for Nakazima test. Reused from [28] with permission through “Copyright Clearance Center”. (B) Schematic of strain measurement method for forming limit diagram using grid pattern.

Figure 1.9. Numerical evaluation of the forming limit diagram. (A) Schematic view of isotropic hardening, kinetic hardening, and combined isotropic kinetic hardening [27]. (B) Schematic view of the yield surface [27].

Figure 1.10. Experimental determination of the limit dome height test. (A) A schematic view of the limit dome height test. (B) A schematic view of deformed limit dome height specimen.

Figure 1.11. Schematic view of certain loading path on Von Mises yield surface.

Figure 1.12. Dependence of stress state on stress triaxiality on the Von Mises yield surface.

Figure 1.13. Tensile necking in a round bar. Reused from [33] with permission through “Copyright Clearance Center”.

Figure 2.1. Overview of Arc melting.

Figure 2.2. Post processing to refine microstructure.

Figure 2.3. Overview of scanning electron microscopy (Tescan Mira3).

Figure 2.4. (A) Dimension of dog-bone shaped for Instron 8801 tensile test machine. (B) Overview of Instron 8801 tensile test machine.

Figure 2.5. (A) Dimension of dog-bone shaped for Instron 5967 tensile test machine. (B) Overview of Instron 5967 tensile test machine.

Figure 2.6. Overview of limit dome height test machine.

Figure 2.7. Schematic view of geometric imperfection of Marciniak-Kuczyski (M-K) model. Reused from [27] with permission through “Copyright Clearance Center”.

Figure 2.8. Finite element model for (A) Central hole test. (B) Notched test.

Figure 2.9. (A) Geometry of central hole test. (B) Geometry of notched test.

Figure 3.1. EBSD maps of the RD-ND cross section of Cantor, TWIP, TRIP, and TaDP CCAs with increasing deformation at room temperature. (A) The main deformation mechanism of Cantor CCA is the dislocation glide as shown in KAM maps. (B) The main deformation mechanisms of TWIP CCA is twinning as shown in IPF maps. (C) The main deformation mechanisms of TRIP CCA is phase transformation as shown in phase maps. (D) The main deformation mechanisms of TaDP CCA is phase transformation as shown in phase maps.

Figure 3.2. Modified tensile test specimen by FE simulation.

Figure 3.3. Tensile behavior of Cantor, TWIP, TRIP, and TaDP CCAs.

Figure 3.4. True stress stress strain curves along the three directions. (A) Cantor, (B) TWIP, (C) TRIP, and (D) TaDP CCAs.

Figure 3.5. Comparison of Swift and Voce hardening law with experimental data. (A) Cantor, (B) TWIP, (C) TRIP, and (D) TaDP CCAs.

Figure 3.6. Yield surface of Von Mises, Hill's 1948, and Yield 2000-2d. (A) Cantor, (B) TWIP, (C) TRIP, and (D) TaDP CCAs.

Figure 3.7. Comparison of forming limit diagram simulated by Marciniak-Kuczyski model with various material characterization. (A) Cantor, (B) TWIP, (C) TRIP, and (D) TaDP CCAs.

Figure 3.8. Determined forming limit diagram of Cantor, TWIP, TRIP, and TaDP CCAs.

Figure 3.9. Comparison of forming limit diagram between commercial alloys and presented CCAs.

Figure 3.10. Photographs of the deformed CCAs: The enlarged photographs of each specimen showed fracture.

Figure 3.11. Force - limit dome height curves of Cantor, TWIP, TRIP, and TaDP CCAs during limit dome height test.

Figure 3.12. Blue and black solid lines represent the uniform elongation in uniaxial tensile test under uniaxial stress state and limit dome height in LDH test

under biaxial stress state, respectively.

Figure 4.1. Fracture specimen after fracture. (A) Central hole test. (B) Notched test.

Figure 4.2. Relation of stress triaxiality and equivalent strain of (A) Central hole test, and (B) Notched test.

Figure 4.3. Relation of stress triaxiality and equivalent strain of TWIP CCA.

Figure 4.4. TWIP CCA is deformed respectively by central hole and notched test up to the same level of equivalent strain = 0.3.

Figure 4.5. Electron channeling contrast image (ECCI) of TWIP CCA by (A) central hole and (B) notched test up to level of equivalent strain = 0.3, revealing thickness of twin is independent by stress state.

Figure 4.6. Relation of stress triaxiality and equivalent strain of TRIP CCA.

Figure 4.7. TRIP CCA is deformed respectively by central hole and notched test up to the same level of equivalent strain = 0.3.

Figure 4.8. Electron backscatter diffraction (EBSD) of TRIP CCA by (A) central hole and (B) notched test up to level of equivalent strain = 0.3.

Figure 4.9. Relation of stress triaxiality and equivalent strain of TaDP CCA.

Figure 4.10. TaDP CCA is deformed respectively by central hole and notched test up to the same level of equivalent strain = 0.3.

Figure 4.11. Electron backscatter diffraction (EBSD) of TaDP CCA by (A) central hole and (B) notched test up to level of equivalent strain = 0.3.

Figure 5.1. Tensile behavior of new CCAs system compared to Cantor, TWIP, TRIP, and TaDP CCAs.

Figure 5.2. EBSD maps of new CCAs system. (A) The main deformation mechanism of CCA19 is the dislocation glide as shown in KAM maps. (B) The main deformation mechanisms of CCA18 is the dislocation glide as shown in KAM maps. (C) The main deformation mechanisms of CCA17 is twinning as shown in IPF maps. (D) The main deformation mechanisms of CCA16 is twinning as shown in IPF maps. (E) The main

deformation mechanisms of CCA15 is twinning as shown in IPF maps. (F) The main deformation mechanisms of CCA13 is twinning as shown in IPF maps. (G) The main deformation mechanisms of CCA12 is phase transformation as shown in phase maps. (H) The main deformation mechanisms of CCA11 is phase transformation as shown in phase maps.

Figure 5.3. Comparison of uniform elongation between new CCAs systems and Cantor, TWIP, TRIP, and TaDP CCAs.

List of Tables

Table 1.1. Stress triaxiality with different stress state.

Table 3.1. Alloy composition used in this study [38].

Table 3.2. Mechanical properties of (A) Cantor, (B) TWIP, (C) TRIP, and (D) TaDP CCAs.

Table 3.3. Comparison of anisotropy factor of each material.

Table 3.4. Fitting parameters of hardening law. (A) Swift hardening law. (B) Voce hardening law.

Table 3.5. The anisotropic coefficient for the (A) Hill's 1948, and (B) Yield 2k-2d.

Table 3.6. Limit dome height value of Cantor, TWIP, TRIP and TaDP CCAs.

Table 5.1. Composition of new designed CCAs.

Chapter 1. Introduction

1.1. Concept of complex concentrated alloys

1.1.1. Definition and characteristics

Historically, metallurgists have developed new alloys, by combining major elements with small amount of minor elements, to modify the microstructure or mechanical properties of material.

Recently, in 2014, new alloy development philosophy, which is known as high entropy alloy (HEA), was proposed by Yeh et al. HEA contains multi principal elements with nearly equiatomic concentrations. Concentration of each elements are between 5 and 35 at.% [2] [3], and all elements act as major elements (Figure 1.1).

Recently, however, there has been considerable interest in nature elements in complex solid solutions compared to their mere numbers. A representative example of this argument is CrCoNi medium entropy-alloy. Exceptional Damage-tolerant properties were found in CrCoNi medium entropy alloy at cryogenic temperatures. It was clearly exceed the excellent cryogenic property of previously reported CrMnFeCoNi high-entropy alloy [4]. Thus, Complex concentrated alloys (CCAs) proposed as new class of alloy derived from a previous research of high entropy alloys (HEAs). Similarly to HEAs, CCAs are also multi-component alloys and often exhibit multi-phase microstructures [5].

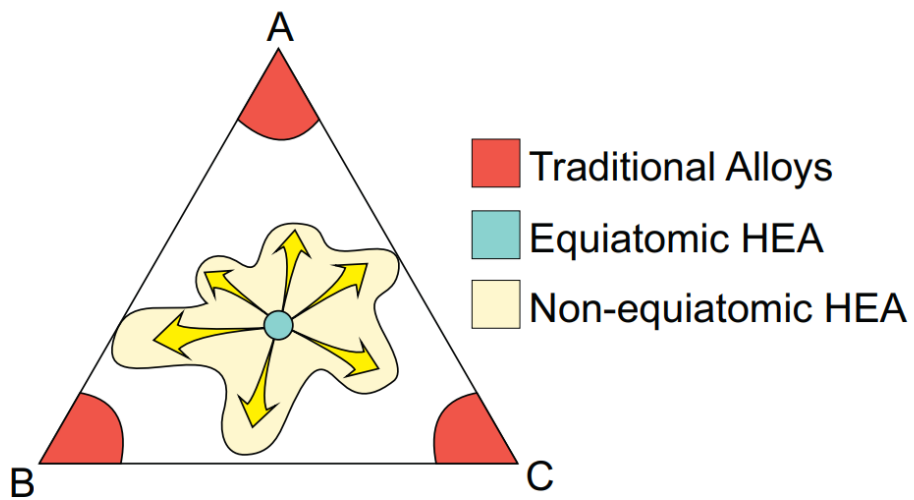


Figure 1.1. Schematic diagram for alloy design of multicomponent system. Reused from [1] with permission through “Copyright Clearance Center”.

1.1.2. Four core effects of complex concentrated alloys

HEAs have demonstrated favorable combination of high fracture toughness [4] [6], outstanding corrosion resistance [7], excellent high-temperature strength [8], and good thermal stability [9]. These exceptional properties are directly related to ‘high entropy’, ‘severe lattice distortion’, ‘sluggish diffusion’, and ‘cocktail effects’, [10] which are now being extended to CCAs.

High entropy effect proposed that when configurational entropy is high enough to overcome enthalpy which tends to develop intermetallic compounds, it tends to stabilize a phase. According to high entropy effect in the equilibrium condition, high configuration entropy be able to lower Gibbs free energy, especially at high temperature. The Gibbs free energy G is

$$G = H - TS, \quad \text{Eq. 1-1}$$

where, H is mixing enthalpy, T is the temperature, and S is the entropy of mixing. In regular solid solution, the configuration entropy of mixing S_{conf} , is as follows:

$$S_{conf} = -R \sum_{i=1}^n X_i \ln X_i, \quad \text{Eq. 1-2}$$

where, R is the gas constant (8.314J/K·mol), n is the components, X_i is mole fractions. According to Eq. 1-2, configuration entropies be able to maximize its value as number of element increases with equi-molar ratios (Figure 1.2). Hence, equi-molar multicomponent alloys be able to lower the Gibbs free energy at high temperature, which encourage formation of stable phases and discourage the formation of intermetallic compounds.

The severe lattice distortion effect [11] is accompanied by large atomic radius differences between neighboring atoms. As a result, atoms exist in non-symmetrical

structure. This can lead to much larger lattice distortion than in conventional alloys, due to misfits in the atomic size and elastic modulus of the solute and solvent atoms. Hence, it causes solid solution strengthening, due to local strain energy which hindered dislocation movement and overall lattice strain associated with binding force.

J.W Yeh et al [12]. studied lattice distortion effect in HEAs by using peak intensity changes in the XRD pattern (Figure 1.3A and Fig 1.3B). The lattice distortion effect decreased the peak intensity of the XRD, beyond the temperature effect (Figure 1.3C).

Sluggish diffusion effect is related to growth of nano size precipitates and formation of new phases. Generally, vacancy concentration for diffusion is limited in substitutional alloy. Vacancy existed in the multi-principal element composition surrounded by different size atoms during diffusion. As a results of lower vacancy mobility multi-principal element composition contribute creep resistance [8].

Figure 1.4 illustrated difference of fluctuation of lattice potential energy during the migration of Ni atom in pure metal, Fe-Cr-Ni, and CoCrFMn_{0.5}Ni. The lattice potential energy (LPE) fluctuation of CCA showed greater value than conventional alloy during atomic migration. In consequence, CCAs have remarkably longer occupation time at a low energy site, resulting lower diffusion rate and sluggish diffusion effect.

Cocktail effect is proposed by S. Ranganathan [13] to emphasize the importance of alloy component to enhance the properties of the materials. This effect indicates that properties of alloy can be modified by the composition of materials.

Al_xCoCrCuFeNi HEA system is introduced to understand cocktail effect.

Addition of aluminum in $Al_xCoCrCuFeNi$ HEA system increases bcc dendrite volume fraction due to stronger cohesive bonding between aluminum and other elements [11]. As a result, the properties effected by all composition of materials. However, each phase consist of multi element solid solution, and its properties come from the interactions of all elements. Therefore, it is important to understand related factors between the elements.

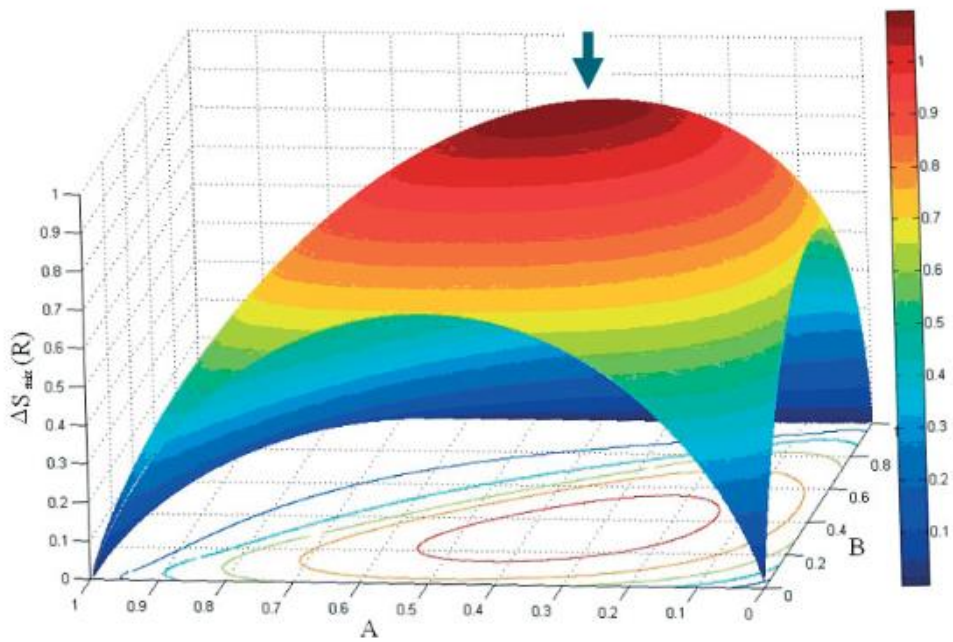


Figure 1.2. Illustration of ΔS_{mix} for ternary alloy system. Reused from [14] with permission through “Copyright Clearance Center”.

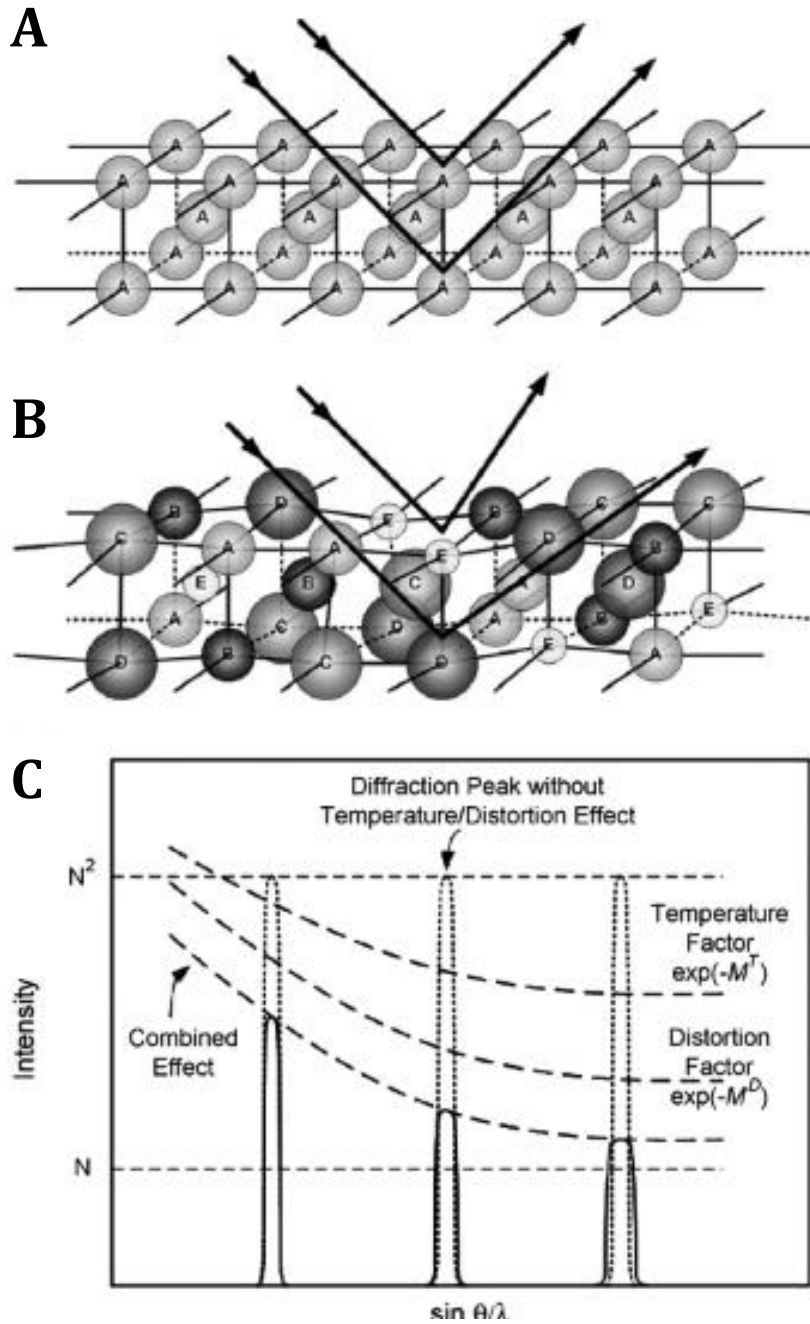


Figure 1.3. Schematic view of severe lattice distortion effects on Bragg diffraction. (A) Perfect lattice with pure alloy. (B) Distorted lattice with multi principal elements. (C) Influence of temperature and distortion effects on the XRD intensity. Reused from [15] with permission through “Copyright Clearance Center” .

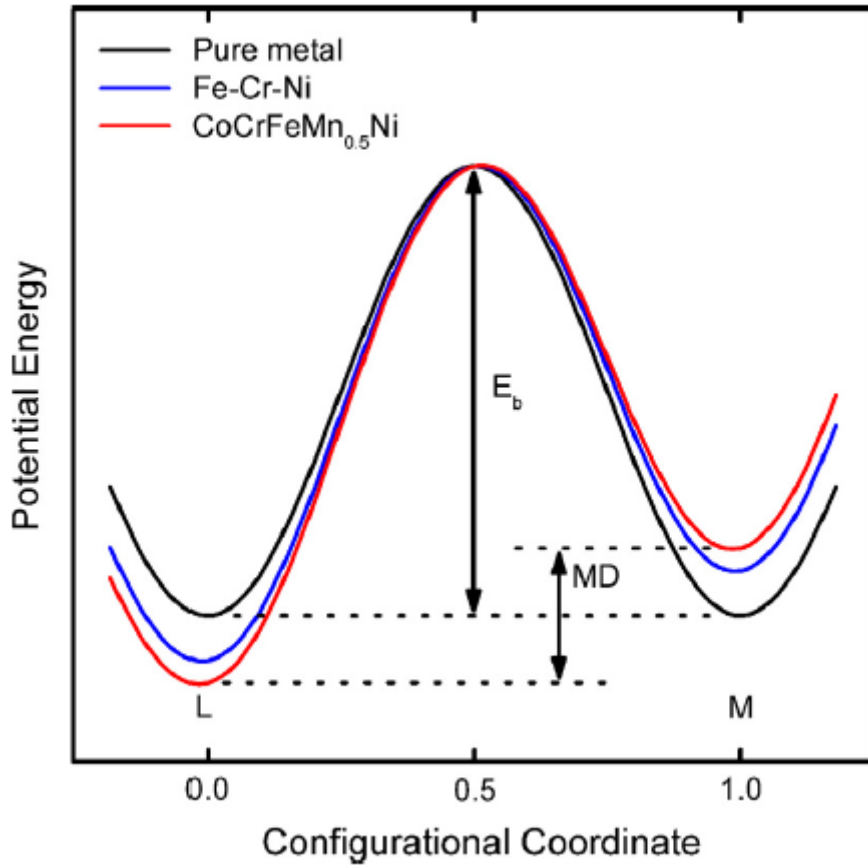


Figure 1.4. Schematic illustration of the difference of fluctuation of lattice potential energy during the migration of Ni atom in different matrices. Reused from [16] with permission through “Copyright Clearance Center” .

1.2. Necessity of evaluation formability

Formability of sheet material means material's ability to be deformed without developing undesirable behavior, and it is very essential property in order to use newly developed alloys as structural materials. Therefore, as shown in (Figure 1.5A, Figure 1.5B), formability evaluation has been performed for commercial alloys.

It is possible to predict the formability of materials from the uniaxial tensile test. In general, it is expected that formability of material would be enhanced at low yield stress and at high ultimate tensile stress, uniform elongation, and strain-hardening exponent. Among them, strain-hardening exponent have great influence on formability. Thus, a better understanding of strain-hardening exponent effect on formability is required.

To understand concept presented above, it is necessary to understand the maximum load and power-law hardening. Load F is expressed as,

$$F = \sigma A, \quad \text{Eq. 1-3}$$

where, σ is stress at a point and A is original plane. At maximum load condition, Eq. 1-3 can be expressed as

$$dF = \sigma dA + A d\sigma = 0, \quad \text{Eq. 1-4}$$

so

$$d\sigma/\sigma = -dA/A = d\varepsilon, \quad \text{Eq. 1-5}$$

or

$$d\sigma/d\varepsilon = \sigma, \quad \text{Eq. 1-6}$$

Since, true strain ϵ is expressed as

$$d\epsilon = d\epsilon/(1 + e), \quad \text{Eq. 1-7}$$

where, e is engineering strain. Substituting Eq. 1-7 into Eq. 1-6, the condition for onset of necking can be expressed as

$$d\sigma/d\epsilon = \sigma/(1 + e). \quad \text{Eq. 1-8}$$

With power-law hardening, Eq. 1-8 can be expressed as

$$d\sigma/d\epsilon = nK\epsilon^{n-1} = \sigma, \quad \text{Eq. 1-9}$$

or

$$\epsilon = n. \quad \text{Eq. 1-10}$$

Eq. 1-10 show strain at onset of necking is equal to strain-hardening exponent. Thus, effective strain at instability are expressed as function of strain-hardening exponent, since strain at onset of necking is equal to strain-hardening exponent [17]. This means strain-hardening exponent is most influential parameter to predict formability from uniaxial tensile test. Although formability is obtained from uniaxial tensile test, real forming processes exhibit multiaxial stress state [18]. Thus, experimental of formability test is necessary.

For example of necessity of formability test is TWIP 940 steel [19]. TWIP 940 steel exhibits large hardening rate and total elongation in uniaxial tensile test. However, during evaluation of formability, TWIP 940 steel failed much earlier than predicted. Chung et al [19]. suggested that major influential factors on this

phenomenon is not only due to failure without strain localization but also due to negative strain rate sensitivity (Figure 1.6A) caused by large strain aging (Figure 1.6B).

As mentioned above, CCAs are attracting so much attention in the industry as a potential promising material, due to excellent mechanical property. However, despite the importance of evaluating formability, most of research conducted on CCAs mainly focused on microstructure analysis [20] and evaluation of mechanical property in uniaxial stress state [21]. Therefore, systematic studies of evaluation of formability on CCAs was conducted in this study.

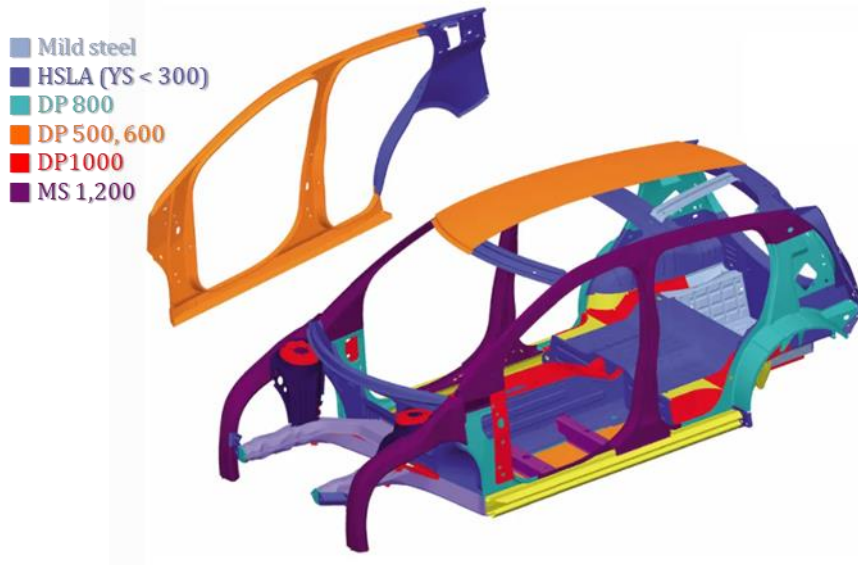
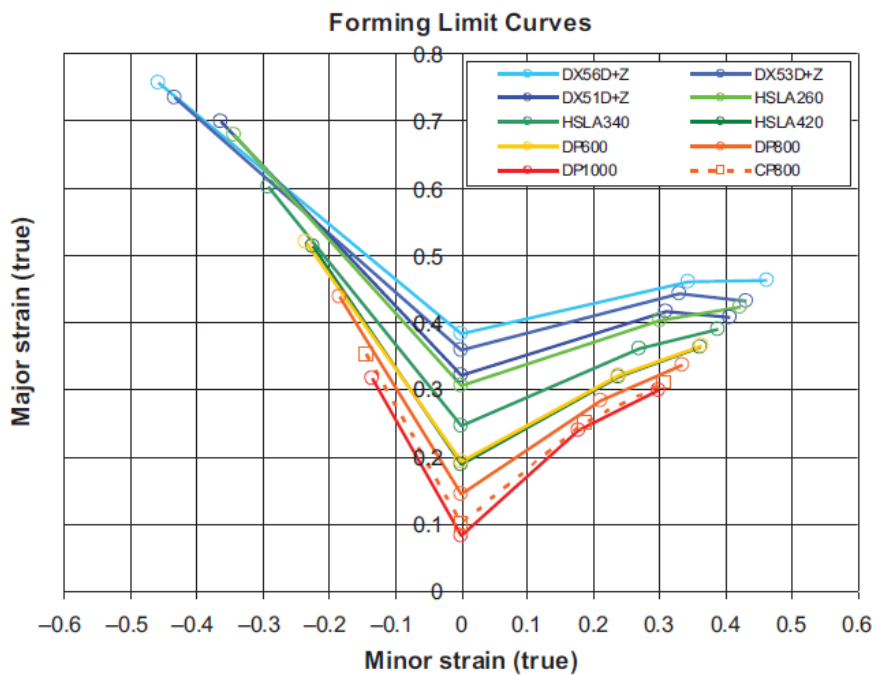
A**B**

Figure 1.5. (A) Example of commercial alloys used in the automotive industry. Reused from [22] with permission through “Copyright Clearance Center”. (B) Overview of forming limit curves for different commercial steel. Reused from [18] with permission through “Copyright Clearance Center”.

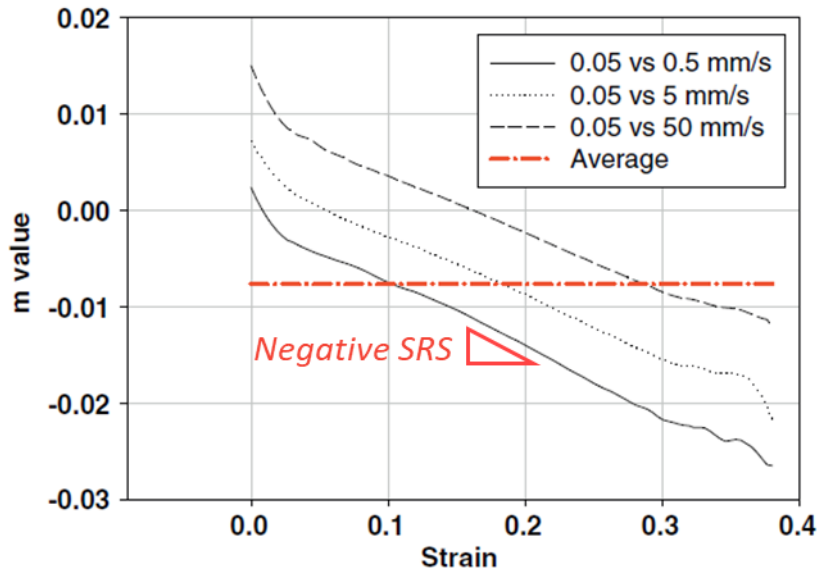
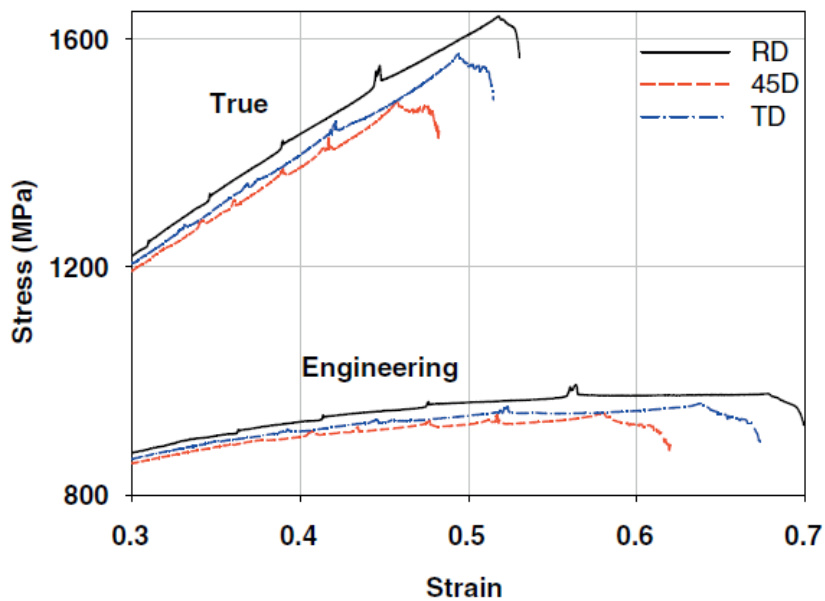
A**B**

Figure 1.6. Mechanical properties of TWIP 940 steel. (A) Variation of the strain rate sensitivity value (m value) of TWIP 940 steel with respect to strain and strain rate. Reused from [19] with permission through “Copyright Clearance Center”. (B) Magnified dynamic strain aging section of tensile curve. Reused from [19] with permission through “Copyright Clearance Center”.

1.3. Measurement of formability

In forming process, sheet specimen suffers 4 deformation modes: deep-drawing, stretching, stretch flanging, and bending [23]. In deep-drawing mode, formed height is obtained by injecting the material in between punch and die. In stretching mode, material is stretched by thinning the material. In stretch flanging mode, material experience tensile deformation by expands cutting edge of material.

In order to evaluate formability of sheet specimen, there are two representative evaluation method. First method is evaluation based on material properties obtained in uniaxial tensile test. Second method is simulative test which conceptually reproduces the deformation mode that the sheet specimen receives.

To evaluate formability through material properties, yield stress, ultimate tensile stress, uniform elongation, strain hardening exponent, and anisotropy factor (R-value) etc. are required.

Representative examples of simulative tests for formability evaluation regarding the 4 types of deformation modes are as follows :

- 1) Deep drawing: evaluation of limit draw ratio (LDR)
- 2) Stretching: evaluation of limit dome height (LDH)
- 3) Stretch flanging: evaluation of hole expansion ratio (HER)
- 4) Bending: bending

Among them, LDH is most frequently used to estimate formability. Therefore, in chapter 1.3.1 illustrated forming limit diagram (FLD) which represents formability by using material properties. In chapter 1.3.2 illustrated the representative simulative test: LDH.

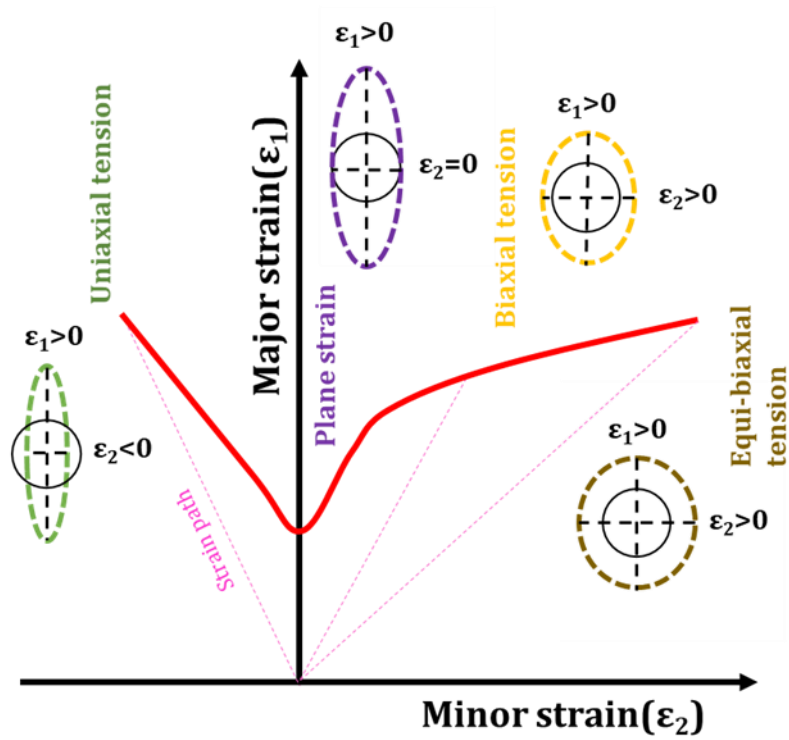


Figure 1.7. Schematic of several major/minor combinations in forming limit diagram [27].

1.3.1. Forming limit diagram

Forming limit diagram (FLD) is a useful concept for indicating formability especially drawability of material. FLD is described in a coordinate system of major (ϵ_1) and minor (ϵ_2) strains. Theoretical prediction of forming limit diagram was firstly proposed by Keeler [24] in 1961. However, Keeler determined only positive range of minor strain. In 1968 Goodwin [25] extended this diagram to the negative range of minor strain. FLD has a typical V-shaped form illustrated as a red solid line in (Figure 1.7). FLD is distinguished into two regions. The region above and below the FLD are called failure region and safe region, respectively.

FLD is experimentally determined by Nakazima forming test [26]. By changing the width of the sheet specimens, major and minor strains in different strain paths are obtained in Nakazima forming test (Figure 1.8A). Strain paths which are demonstrated as pink dotted lines in Figure 1.7 are represented as,

$$\rho = \epsilon_2 / \epsilon_1, \quad \text{Eq. 1-11}$$

As deformation occurs, major and minor strains increase along the strain path. To measure major and minor strains, circular grid patterns were applied on the surface of the specimens. During the test, the specimens were deformed until onset of fracture by a hemispherical punch. Major and minor strains are measured from the deformed grid pattern which is located nearest to the fracture line, which is called localized necking (Figure 1.8B). When all the measurements and evaluations are completed, the fracture points of various strain paths are followed simultaneously.

However, experimentally measuring FLD requires a large amount of experiments, and even in the same material, different experimental results can be obtained, due to the difference in thickness or surface roughness of the specimen.

Therefore, recently FLD has been constructed through simulation.

As mentioned previous section, the determination of FLD by simulation required many parameters from uniaxial tensile test, such as yield stress, ultimate tensile stress, uniform elongation, strain hardening exponent, and anisotropy factor (R-value) etc. The yield surface concept provides the connection between uniaxial and multiaxial stress state. Therefore, determine yield surface is most important concept to predict FLD.

As the deformation progresses, the size and shape of the yield surface changed (Figure 1.9A). If the expansion of yield surface occurs without changing shape and position, it is well known as isotropic hardening. If yield surface only moved its position without changing the size or shape, it is well known as kinematic hardening. By combining the isotropic and kinematic hardening, the Bauschinger effect can be described. It is called, combined isotropic-kinematic hardening. It is essential to set combined isotropic kinematic hardening for the material. Representative example of hardening laws are Ludwick, Hollomon, Swift, and Voce hardening law.

The shape of the yield surface could be changed depending on the anisotropy properties of the materials as shown in Figure 1.9B. Thus, by determining anisotropic yield function of materials, anisotropic effective plastic strain increment could be obtained as deformation progresses. Representative example of Yield surfaces are Von Mises, Hill1948, Yield 2000 anisotropy yield criteria.

As a result, FLD can be constructed, because the effective plastic strain increment in multiaxial stress state could be estimated from the parameters obtained from uniaxial stress state by determining the hardening law and anisotropy yield surface for the material [27].

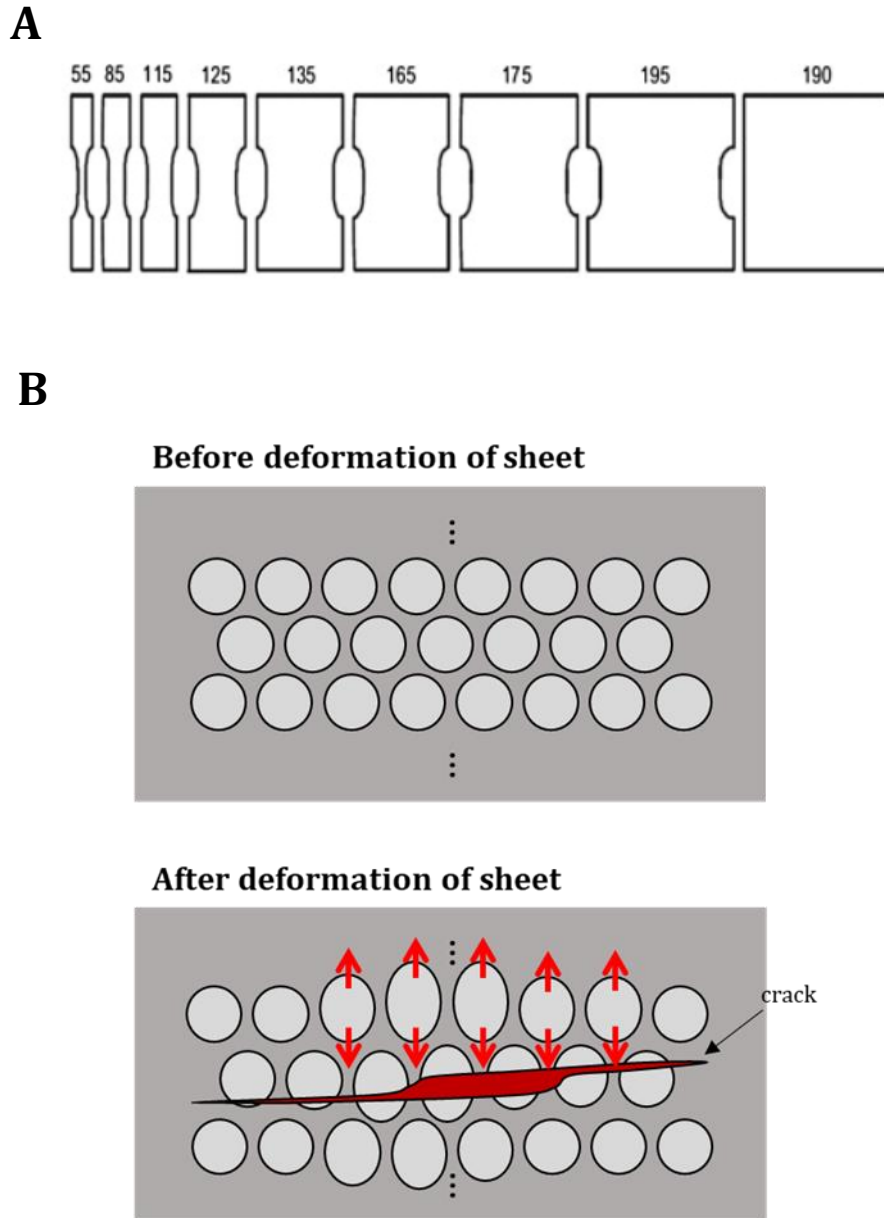


Figure 1.8. Experimental determination of the forming limit diagram. (A) Schematic of sample dimension used for Nakazima test. Reused from [28] with permission through “Copyright Clearance Center”. (B) Schematic of strain measurement method for forming limit diagram using grid pattern.

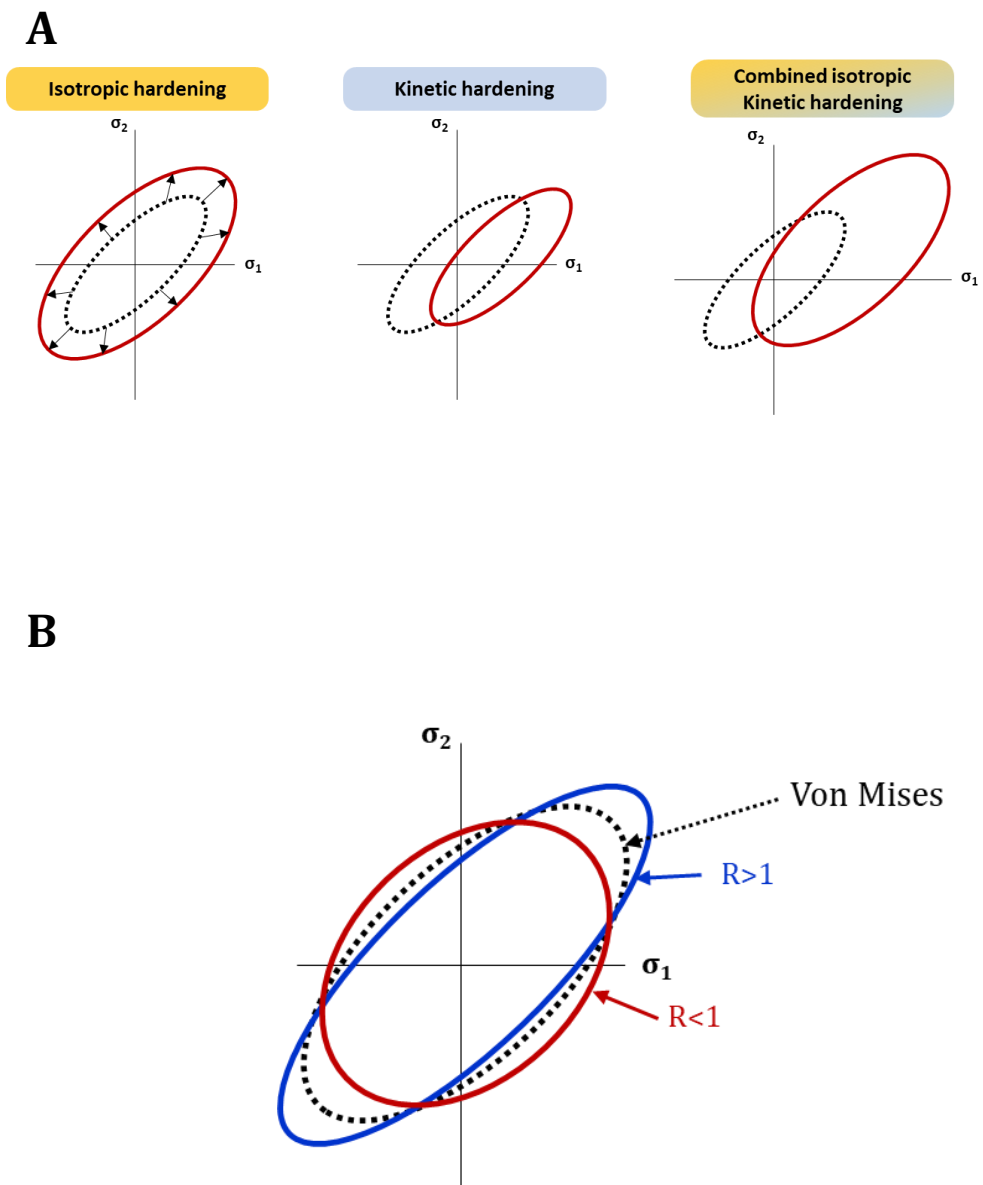


Figure 1.9. Numerical evaluation of the forming limit diagram. (A) Schematic view of isotropic hardening, kinetic hardening, and combined isotropic kinetic hardening [27]. (B) Schematic view of the yield surface [27].

1.3.2. Limit dome height test

In industry applications of sheets, stretchability of a metal is measured as the resistance to localized necking or fracture. It is evaluated by limit dome height (LDH) test. The LDH test developed extensively [29] [30], due to good correlation to industrial failure.

LDH test also deformed material until fracture by hemispherical punch (Figure 1.10A), and results are described in coordinate system of force (N) and limit dome height (mm). Generally, high strength materials exhibit greater force and materials with better plasticity show greater Limit dome height.

The dome height of deformed specimen is defined as limit dome height (Figure 1.10B). The formability of the material is evaluated by comparing the limit dome height value. Material with high limit dome height value is evaluated as better formability material.

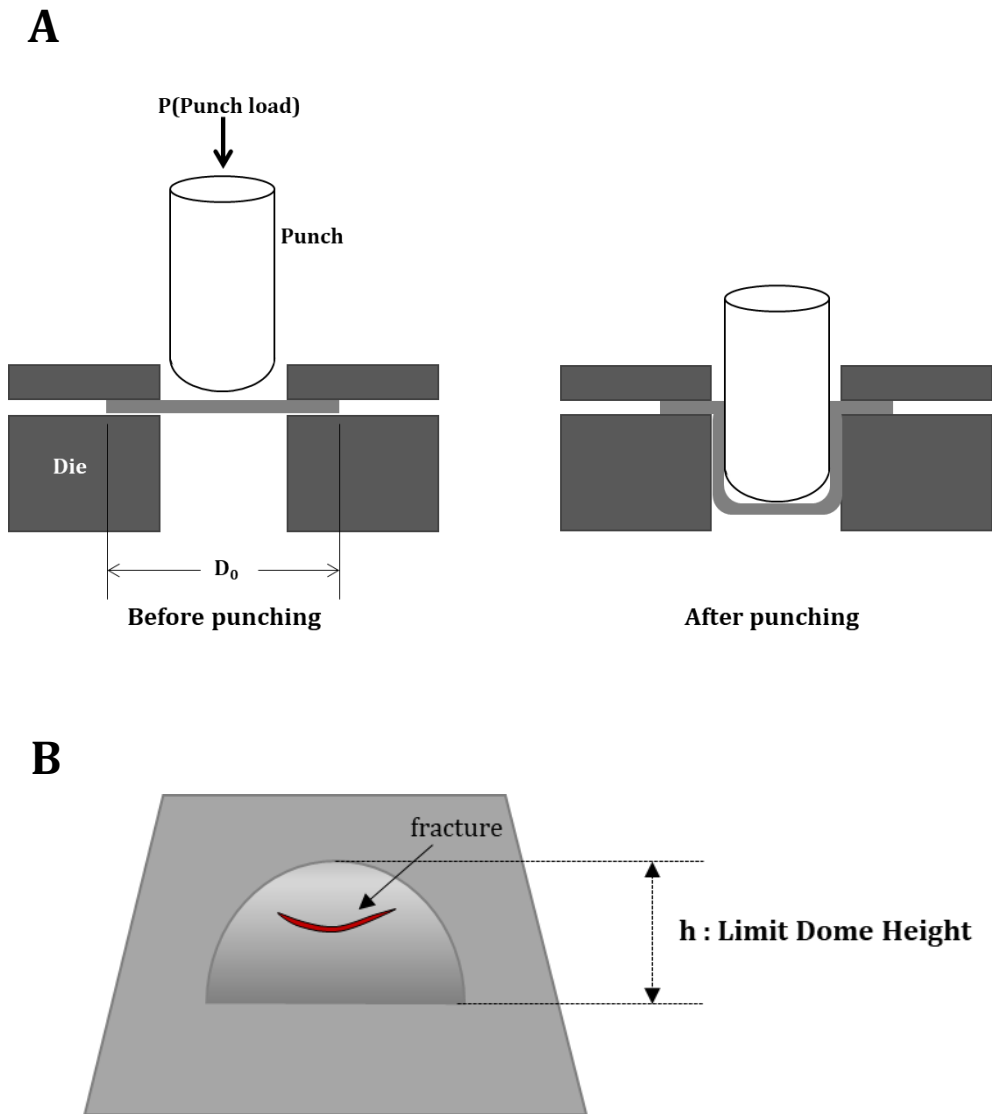


Figure 1.10. Experimental determination of the limit dome height test. (A) A schematic view of the limit dome height test. (B) A schematic view of deformed limit dome height specimen.

1.4. Stress state analysis

1.4.1. Concept of triaxiality

Multiaxial stress states are exhibited in real forming processes. In particular, it is known that not only uniaxial stress state but also plane and biaxial stress states occurred in the forming process (Figure 1.11). Therefore, it is essential to understand the deformation behavior in each stress state.

Stress triaxiality is commonly used as a parameter representing stress state. It is defined as ratio of hydrostatic stress and Von Mises equivalent stress [31]. Stress triaxiality η is

$$\eta = \frac{\sigma_m}{\sigma_{eq}}, \quad \text{Eq. 1-12}$$

where, σ_m is hydrostatic stress and σ_{eq} is Von Mises equivalent stress. Hydrostatic stress has form as

$$\sigma_m = \frac{1}{3}(\sigma_1 + \sigma_2 + \sigma_3), \quad \text{Eq. 1-13}$$

where, σ_1 , σ_2 , and σ_3 are principal stresses. Von Mises equivalent stress is represented as

$$\sigma_{eq} = \frac{1}{\sqrt{2}}\sqrt{(\sigma_1 - \sigma_2)^2 + (\sigma_2 - \sigma_3)^2 + (\sigma_3 - \sigma_1)^2}, \quad \text{Eq. 1-14}$$

Figure 1.12 shows the stress triaxiality represents the stress state as scalar value. The stress triaxiality for different stress state are listed in Table 1.

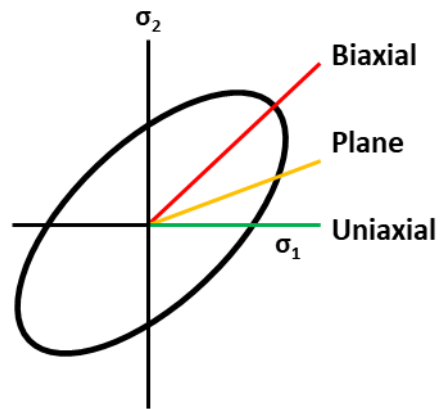


Figure 1.11. Schematic view of certain loading path on Von Mises yield surface.

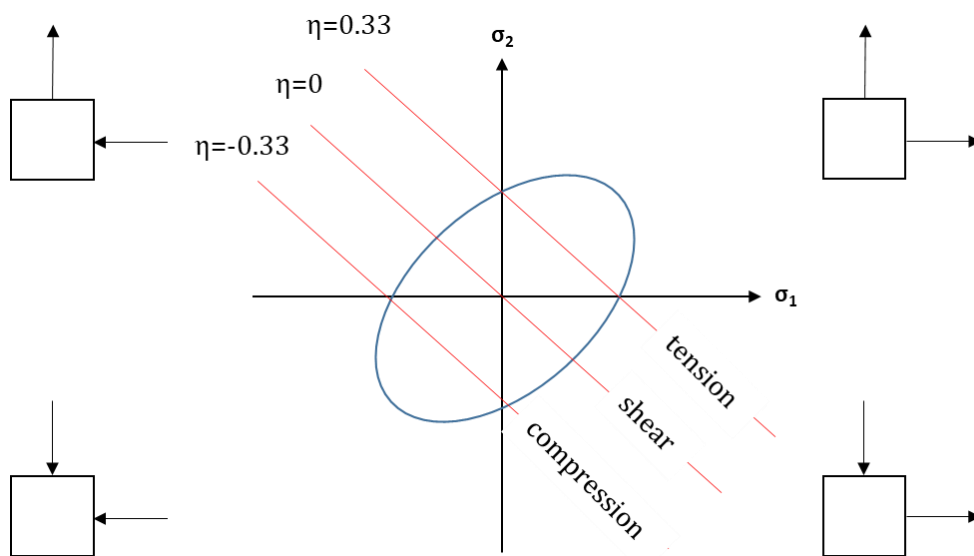


Figure 1.12. Dependence of stress state on stress triaxiality on the Von Mises yield surface.

Table 1.1. Stress triaxiality with different stress state

| Stress state | η |
|----------------------|--------------------------|
| Uniaxial tension | 0.33 |
| Equi-biaxial tension | 0.67 |
| Plane strain tension | 0.58 |
| Simple shear | 0 |

1.4.2. Fracture test

In 1952, Bridgman [32] presents that stress triaxiality, which represents stress state at the center of the specimen, based on the specimen geometry (Figure 1.13).

The stress triaxiality determined by specimen geometry is

$$\eta = \frac{\sigma_m}{\sigma_{eq}} = \frac{1}{3} + \ln\left(1 + \frac{a}{2R}\right), \quad \text{Eq. 1-15}$$

where, a and R are radius of minimum cross section. Bridgman method clearly depends on the initial dimension, a and R . Therefore, stress state could be determined according to the geometric relation.

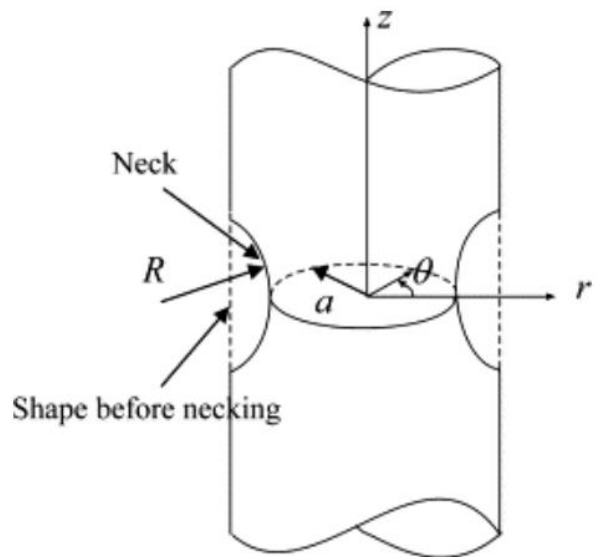


Figure 1.13. Tensile necking in a round bar. Reused from [33] with permission through "Copyright Clearance Center".

1.5. Motivation and scope

CCAs are attracting so much attention in the industry as a potential promising material, due to its excellent mechanical properties in uniaxial stress state. However, real forming process exhibits not only uniaxial stress state but also multi stress state. Also, due to various parameters such as strain rate sensitivity, anisotropy, stress state, and microstructure etc., the formability of material could have different tendency with uniaxial stress state property. Therefore, evaluation of formability is indispensable for the new composition alloy to be used as a structural material. For this reason, evaluation of formability has been performed for all commercial alloys (Figure 1.5A, 1.5B). However, in spite the importance, evaluation of formability has not been reported.

Hence, in this thesis, CCAs compositions with different deformation mechanisms were selected to evaluate formability systematically. To effectively proceed with evaluation of formability, following strategy was done,

- 1) Construct a forming limit diagram (FLD) of each material through the hardening law and anisotropy yield surface obtained from the uniaxial tensile test. Through this, drawability mode of formability is evaluated.
- 2) Simulate test of real forming process is performed through Limit dome height (LDH) test. Through this, stretchability mode of formability is evaluated.
- 3) Compare the deformation tendency of materials between uniform elongation, which represents uniaxial stress state, and limit dome height,

which represents uni-biaxial stresses state.

- 4) Finally, in order to understand the real forming process of materials, microstructure analysis would be conducted in the various stress state.

To satisfy the requirements of the research strategies, first, systematically control the stacking fault energy (SFE) to change deformation mechanism of materials. Second, uniaxial tensile test was carried out to determine hardening law and anisotropy yield criteria for materials. Third, forming limit diagram of CCAs with different deformation mechanisms are carefully constructed by simulation. Then, limit dome height test was carried out which exhibits real forming process. Finally, fracture test was employed for comparing deformation behavior of uniaxial stress state and plane stress state which is most frequently occurs during forming process.

Chapter 2. Experimental procedure

2.1. Sample preparation

Master alloy ingots were prepared by arc or induction melting depending on the purposes. Induction melting was used to manufacture large samples for formability test. Arc melting was used to quickly manufacture the newly designed alloys. To optimize the microstructure, as-cast ingots were post processed as followed, to optimize the microstructure.

2.1.1. Casting procedure

Induction melting: 6kg of alloys were casted in alumina crucible (130 mm(OD) x 150 mm(H)) under Ar atmosphere. The molten metals were then poured into carbon mold. High purity elements above 99.95% were used in induction melting. This method was employed to manufacture large sample.

Arc melting: 40g of mater alloy buttons were prepared by arc melting using high purity (>99.9%) Cr, Mn, Fe, Co, and Ni under Ti-gettered Ar atmosphere. Overview of Arc melting is shown in Figure 2.1. The buttons were re-melted at least five times to improve chemical homogeneity of alloys. Thereafter, buttons were drop casted into the water-cooled copper mold (16mm x 6mm x 51mm).



Figure 2.1. Overview of Arc melting.

2.1.2. Post processing

Homogenization: The as cast ingots were homogenized to remove the elemental segregation. The as cast ingot was homogenized at 1100°C for 36 hours in air atmosphere, followed by furnace cooling. Arc melted ingot was homogenized at 1100°C for 24 hours in air atmosphere, followed by water quenching (Figure 2.2).

Grain refinement: Homogenized samples were cold rolled with rolling reduction ratio of 30%. After that, samples were annealed at 900°C for 1 hour in air atmosphere, followed by water quenching. Annealed samples were cold rolled with reduction ratio of 50%. Finally, recrystallization process, 900°C for 5min or 7min depending on composition, was conducted (Figure 2.2).

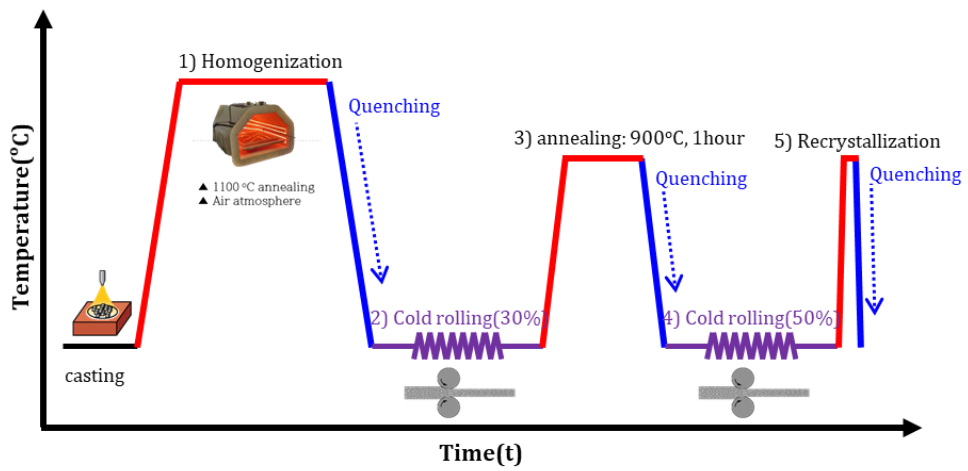


Figure 2.2. Post processing to refine microstructure.

2.2. Microstructural characterization

Microstructure characterization was carried out on recrystallized and deformed sample. Secondary electron (SE) imaging, electron backscatter diffraction (EBSD), and electron channeling contrast imaging (ECCI) were conducted in a Tescan Mira3 scanning electron microscope (SEM) equipped with an XFlash 6130 Bruker EDS and Quantax EBSD detector (Figure 2.3).



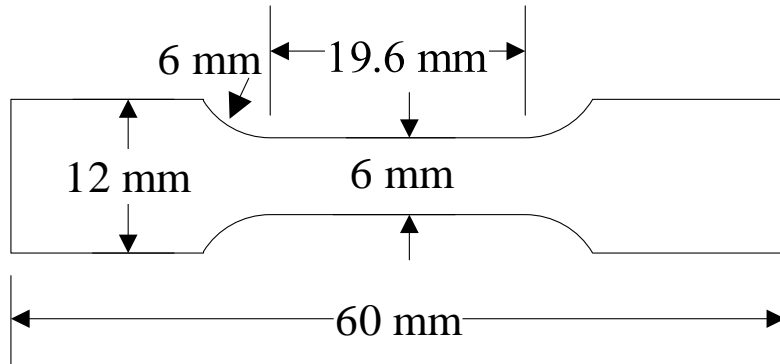
Figure 2.3. Overview of scanning electron microscopy (Tescan Mira3).

2.3. Mechanical analysis

2.3.1. Uniaxial tensile test

Two types of dog-bone shaped specimens are prepared by electrical discharge machining (EDM). Tensile tests were performed on Instron 8801 and Instron 5967, gauge length of the tensile specimens were 12 mm and 8~10 mm, respectively. The size and shapes of the samples were determined depending on the purpose of the tensile tests. Uniaxial tensile tests were carried out at room temperature and strain rate of $1 \times 10^{-3} \text{S}^{-1}$. The strain measurement was measured by digital image correlation (DIC) for Instron 8801, and AVE camera for Instron 5967.

A



B

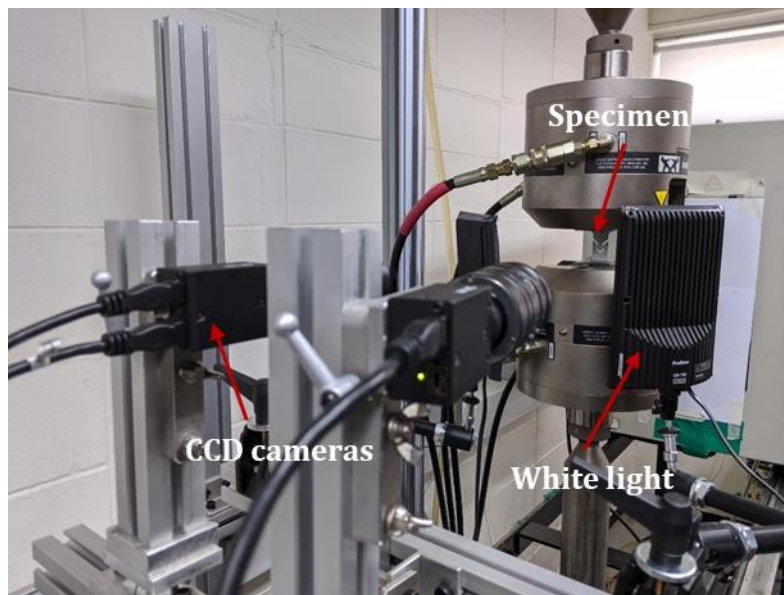
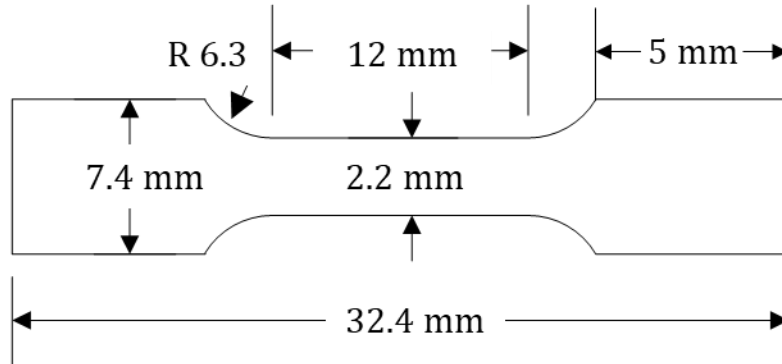


Figure 2.4. (A) Dimension of dog-bone shaped for Instron 8801 tensile test machine. (B) Overview of Instron 8801 tensile test machine.

A



B

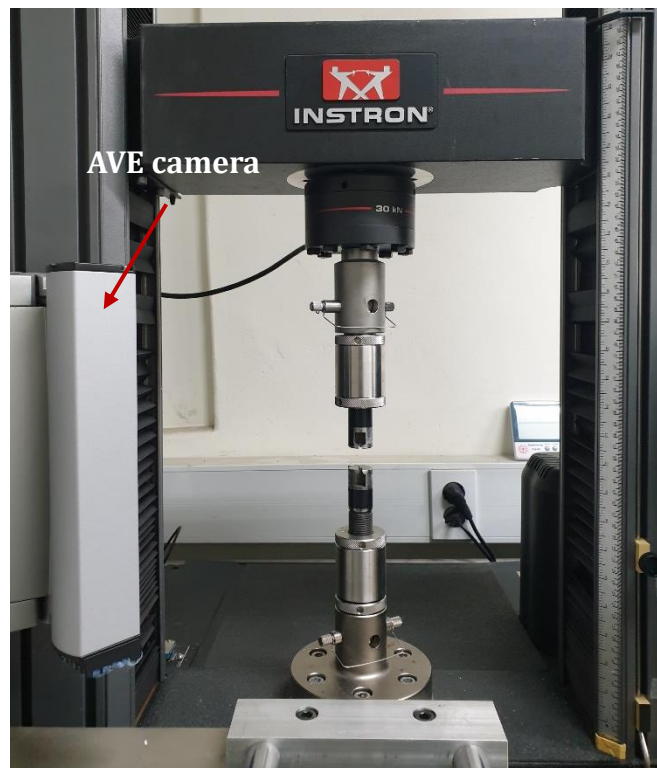


Figure 2.5. (A) Dimension of dog-bone shaped for Instron 5967 tensile test machine. (B) Overview of Instron 5967 tensile test machine.

2.3.2. Limit dome height test

Limit dome height test carried out with a punch speed 10^{-2} mm/sec at room temperature. The diameter of the hemispherical punch was 20mm. Overview of limit dome height test machine is shown in Figure 2.6. The limit dome height machine was equipped with Instron 5582, 100KN load cell capacity. The specimens were prepared with dimensions of 55 mm x 55 mm (length x width). Silicone lubricant was used to minimize friction between specimen and punch.

The limit dome height test was performed until a punch force decreased. The depth of the punch is generally defined as limit dome height (LDH).



Figure 2.6. Overview of limit dome height test machine.

2.4. Calculation method of forming limit diagram

Marciniak and Kuczyski (M-K) model is used to predict forming limit diagram (FLD). M-K assumes initial imperfection as shown in Figure 2.7. In Figure 2.7, region a is homogeneous region and region b is imperfection region. The initial imperfection is characterized by the thickness ratio. Initial imperfection is followed by,

$$f_i = t_b/t_a, \quad \text{Eq. 2-1}$$

where, t_b is thickness of imperfection region and t_a is thickness of homogeneous region. In this study, 0.996 of instability factor, which represents thickness ratio, is used to predict FLD.

Compatibility condition is required at the interface. Therefore, initially, deformation at region a and b is same. However, when plastic flow occurs, evolution of strain rate is different in the two regions, due to thickness of region b is thinner than region a. When strain increments in imperfection region 2 ($d\bar{\varepsilon}^b$) is ten times greater than homogeneous region 1 ($d\bar{\varepsilon}^a$), M-K model assumes that the strain localization occurs.

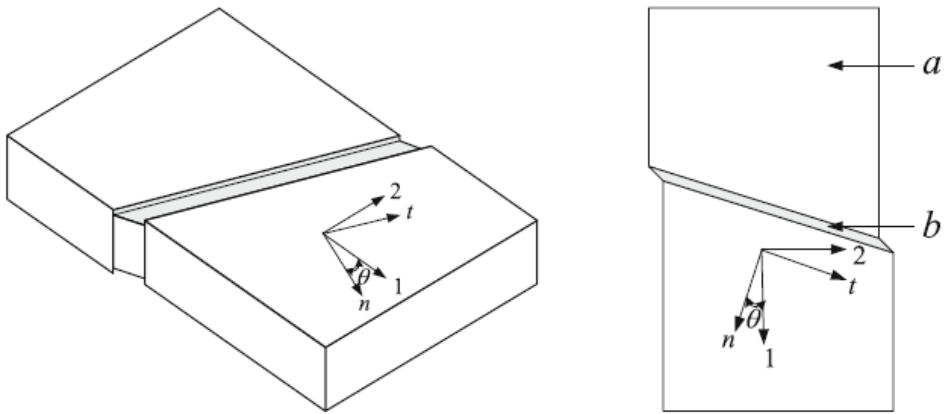


Figure 2.7. Schematic view of geometric imperfection of Marciniak-Kuczyski (M-K) model. Reused from [27] with permission through “Copyright Clearance Center”.

2.5. Simulation method of stress state analysis

The fracture test was conducted to compare the deformation behavior according to stress state. FE software Abacus was used to validate stress triaxiality. 8 node brick element with reduced integration (C3D8R) was used as element type. Element size at critical point is 0.05mm x 0.05mm x (thickness/16). Number of elements are 14672 for central hole and 17632 for notched test, and Number of nodes are 16853 and 20032 for central hole and notched test, respectively (Figure 2.8). The geometry of central hole test is shown in Figure 2.9A, and geometry of notched test is shown in Figure 2.9B. The specimens were clamped at Instron 8801 tensile test machine at a strain rate of 1mm/min. Digital image correlation (DIC) virtual extensometer with 20mm gauge length was used for displacement analysis and conventional axial extensometer with 25mm gauge length was attached for interrupt test.

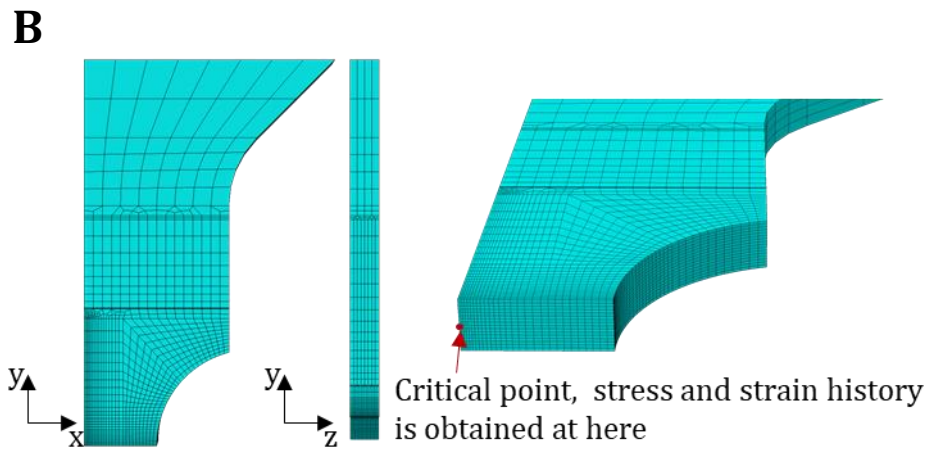
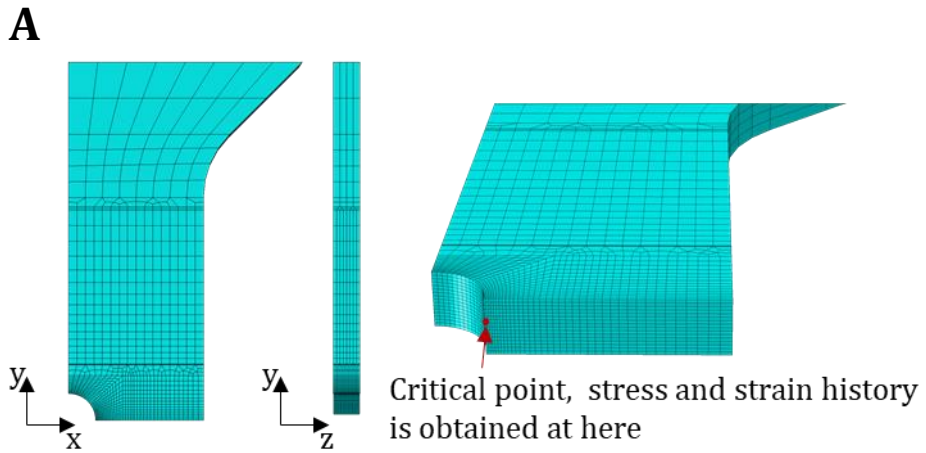


Figure 2.8. Finite element model for (A) Central hole test. (B) Notched test.

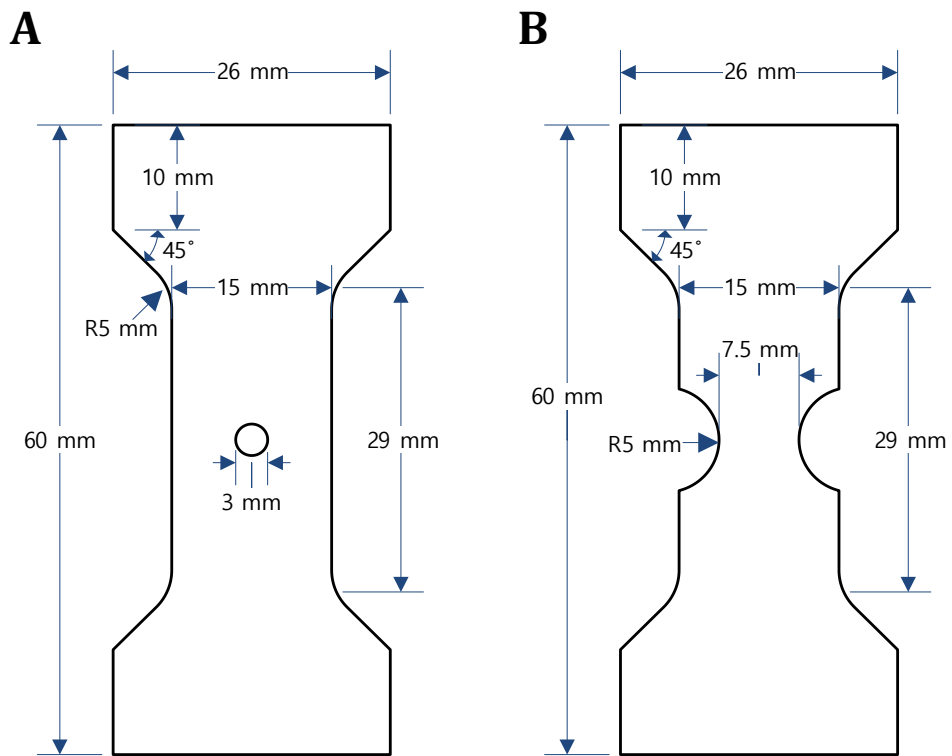


Figure 2.9. (A) Geometry of central hole test. (B) Geometry of notched test.

Chapter 3. Formability of complex concentrated alloys with different deformation mechanism

3.1. Deformation mechanism difference depending on stacking faults energy

In face centered cubic (FCC), (111) planes are stacked on a sequence ABCABC $(a_0/2)[\bar{1}10]$ is well known as slip direction in FCC crystal, and it is called perfect dislocation. Shear displacement can be accomplished by shear of Shockley partial dislocation along every other $[29]$ plane. Perfect dislocation decomposed into two partial dislocations. This phenomenon is expressed as,

$$\frac{a_0}{2} [\bar{1}10] \rightarrow \frac{a_0}{6} [\bar{1}2\bar{1}] + \frac{a_0}{6} [\bar{2}11]. \quad \text{Eq. 3-1}$$

The above reaction means perfect dislocation dissociated into two partial dislocations, and this process creates stacking fault [34-36]. The region between two partial dislocations, stacking fault energy (SFE) exist. SFE has greatest influence on determining the deformation mechanism of FCC crystals. Main deformation mechanism of FCC crystal with high SFE is dislocation gliding. On the other hand, secondary deformation mechanism (mechanical twinning and martensitic transformation) is prevalent in FCC crystal with low SFE, due to wide stacking faults which hindered dislocation gliding.

Olson and Coshen [37] proposed stacking fault energy as,

$$\Gamma = 2\rho\Delta G^{\gamma \rightarrow \varepsilon} + 2\sigma^{\gamma/\varepsilon} \quad \text{Eq. 3-2}$$

Where, Γ is stacking fault energy, ρ is molar surface density along $[29]$, $\Delta G^{\gamma \rightarrow \varepsilon}$ is molar Gibbs energy of austenite (γ) to martensite (ε), phase

transformation, and $\sigma^{\gamma/\varepsilon}$ is surface energy of γ and ε interface. Thus, FCC austenite phase can be manipulated by changing composition of alloy.

Therefore, to study the formability of FCC CCAs for various deformation mechanisms, composition of alloys were changed. In order to cause secondary mechanisms during deformation, the Mn and Ni contents, which are generally known to increase SFE, are reduced, and the Fe and Co contents which are known to lower SFE are increased.

3.2. Microstructure prior to the deformation

In order to evaluate the formability of complex concentrated alloys (CCAs), the formability evaluation is performed not only for Cantor alloys that dislocation gliding during plastic flow but also for secondary deformation CCAs during plastic flow.

In this thesis, the composition shown in Table 3.1 [38] was studied to identify the formability tendency of CCAs depending on deformation mechanisms. In Figure 3.1, microstructural evolution during limit dome height (LDH) test was investigated using electron backscattered diffraction (EBSD) to verify deformation mechanisms of CCAs.

The equivalent strains for deformed specimens after the LDH test were different with respect to the specimen position. Thus, RD-ND cross-section of each specimen were divided into three regions (Bottom, bending, and dome). Bottom, bending and dome are unreformed, deformed severely deformed region, respectively. Therefore, the microstructure in the bottom, bending and dome regions were analyzed to determine the deformation mechanism of each alloys.

Figure 3.1A gives kernel average misorientation (KAM) maps of $\text{Cr}_{20}\text{Mn}_{20}\text{Fe}_{20}\text{Co}_{20}\text{Ni}_{20}$, which is known as Cantor alloy. These data reveal that Cantor alloy has dislocation gliding as deformation mechanism.

Figure 3.1B gives inverse pole figure (IPF) maps of $\text{Cr}_{20}\text{Mn}_{14}\text{Fe}_{26}\text{Co}_{26}\text{Ni}_{14}$. In the bending region, very few mechanical twins are observed. In the dome region, lots of mechanical twins are observed, which is evidence of twin-induced plasticity mechanism. Therefore, this composition noted as TWIP (twinning induced plasticity)

CCA.

Figure 3.1C gives phase maps of $\text{Cr}_{20}\text{Mn}_{10}\text{Fe}_{30}\text{Co}_{30}\text{Ni}_{10}$. In the bottom region, reveals that γ - austenite single phase microstructure. In the bending and dome region, ϵ martensite are observed with austenite phase, which means that large amount of deformation is driven by the phase transformation. Therefore, this composition noted as TRIP (transformation induced plasticity) CCA.

Figure 3.1D gives phase maps of $\text{Cr}_{20}\text{Mn}_8\text{Fe}_{32}\text{Co}_{32}\text{Ni}_8$. In the bottom region, reveals a few ϵ martensite with austenite. In the bending and dome region, lots of ϵ martensite are observed with austenite phase, which means that large amount of deformation is driven by the phase transformation. Through these results, initial microstructure is dual phase and deformation mechanism is phase transformation. Therefore, this composition is noted as TaDP (TRIP-assisted dual phase) CCA.

Table 3.1. Alloy composition used in this study [38].

| | Composition | ΔG (hcp-fcc)(J) |
|---|--|---|
| 1 | $\text{Cr}_{20}\text{Mn}_{20}\text{Fe}_{20}\text{Co}_{20}\text{Ni}_{20}$ | 1927.8 |
| 2 | $\text{Cr}_{20}\text{Mn}_{14}\text{Fe}_{26}\text{Co}_{26}\text{Ni}_{14}$ | 771.0 |
| 3 | $\text{Cr}_{20}\text{Mn}_{10}\text{Fe}_{30}\text{Co}_{30}\text{Ni}_{10}$ | 245.3 |
| 4 | $\text{Cr}_{20}\text{Mn}_8\text{Fe}_{32}\text{Co}_{32}\text{Ni}_8$ | 59.4 |

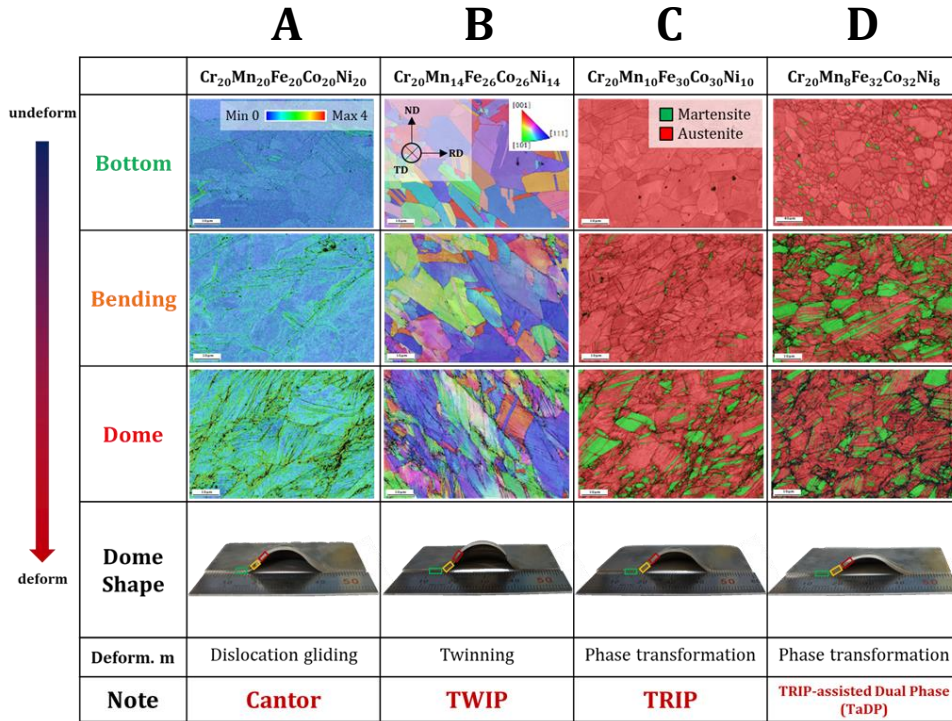


Figure 3.1. EBSD maps of the RD-ND cross section of Cantor, TWIP, TRIP, and TaDP CCAs with increasing deformation at room temperature. (A) The main deformation mechanism of Cantor CCA is the dislocation glide as shown in KAM maps. (B) The main deformation mechanisms of TWIP CCA is twinning as shown in IPF maps. (C) The main deformation mechanisms of TRIP CCA is phase transformation as shown in phase maps. (D) The main deformation mechanisms of TaDP CCA is phase transformation as shown in phase maps.

3.3. Uniaxial tensile test

3.3.1. Uniaxial tensile test depending on rolling direction

Uniaxial tensile test for the current CCAs with various SFE are carried out. The tensile specimens were fabricated according to modified ASTM E8 by FE simulation. Figure 3.2. shows that homogeneous deformation occurs in gauge length region.

At least three specimens were prepared along the rolling direction by electrical discharge machining (EDM). Instron 8801 test machine, 100KN load cell capacity, was used for testing. Stereo digital image correlation (DIC) was used in all test to measure strain. Specimens were loaded at a strain rate of $1 \times 10^{-3} \text{ s}^{-1}$ at room temperature.

As for Cantor CCA, the uniform elongation (ϵ_u) was 0.32 and ultimate tensile strength (UTS) was close to 679 MPa. For TWIP CCA, ϵ_u was 0.45 and UTS was 699 MPa. For TRIP CCA, ϵ_u was 0.46 and UTS was 798 MPa. For TaDP CCA, ϵ_u was 0.42 and UTS was 870 MPa. While yield strength (σ_y) of current CCAs exhibits similar to each other at $\sim 300 \text{ MPa}$ (Figure 3.3).

From the above results, UTS and ϵ_u increases from Cantor to TWIP to TRIP CCAs, and ϵ_u decreased in TaDP CCA. However, TaDP shows considerably higher strain hardening tendency over the entire plastic deformation region among them.

As mentioned in chapter 1.2, strain-hardening exponent is most influential parameter for predict formability from uniaxial tensile test. Hence, TaDP CCA is predicted to have the best formability among other alloys.

As for anisotropy property for each specimen, uniaxial test along the rolling

direction are conducted. Figure 3.4 shows true stress strain curve along the rolling direction. Applied loading axis are rolling direction (RD), transverse direction (TD), or 45° off from the rolling direction (45D). Each direction exhibited almost identical stress strain curves. The mechanical properties are summarized in Table 3.2.

As for the elastic properties, ultrasonic technique was used to measure young's modulus and Poisson's ratio of each material. The ultrasonic waves were recorded by a Tektronix 220 oscilloscope. Measured young's modulus and Poisson's ratio along the rolling direction are listed in Table 3.2.

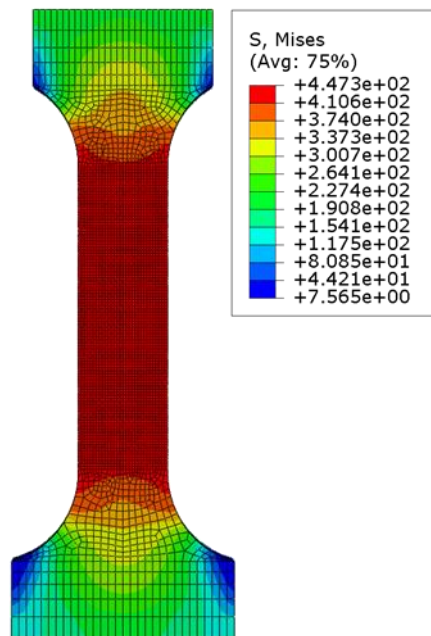


Figure 3.2. Modified tensile test specimen by FE simulation.

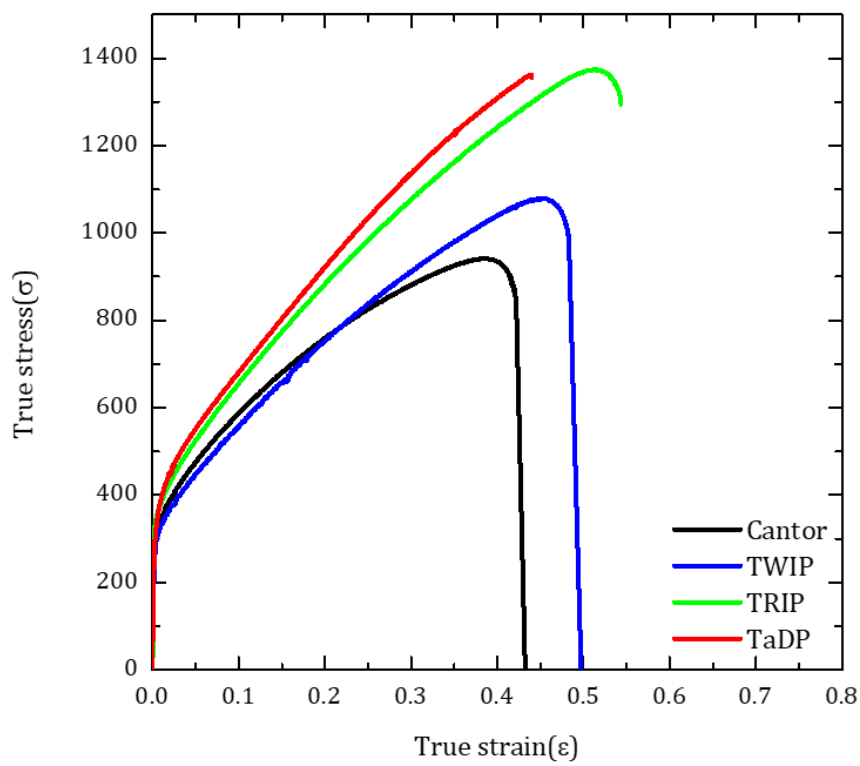


Figure 3.3. Tensile behavior of Cantor, TWIP, TRIP, and TaDP CCAs.

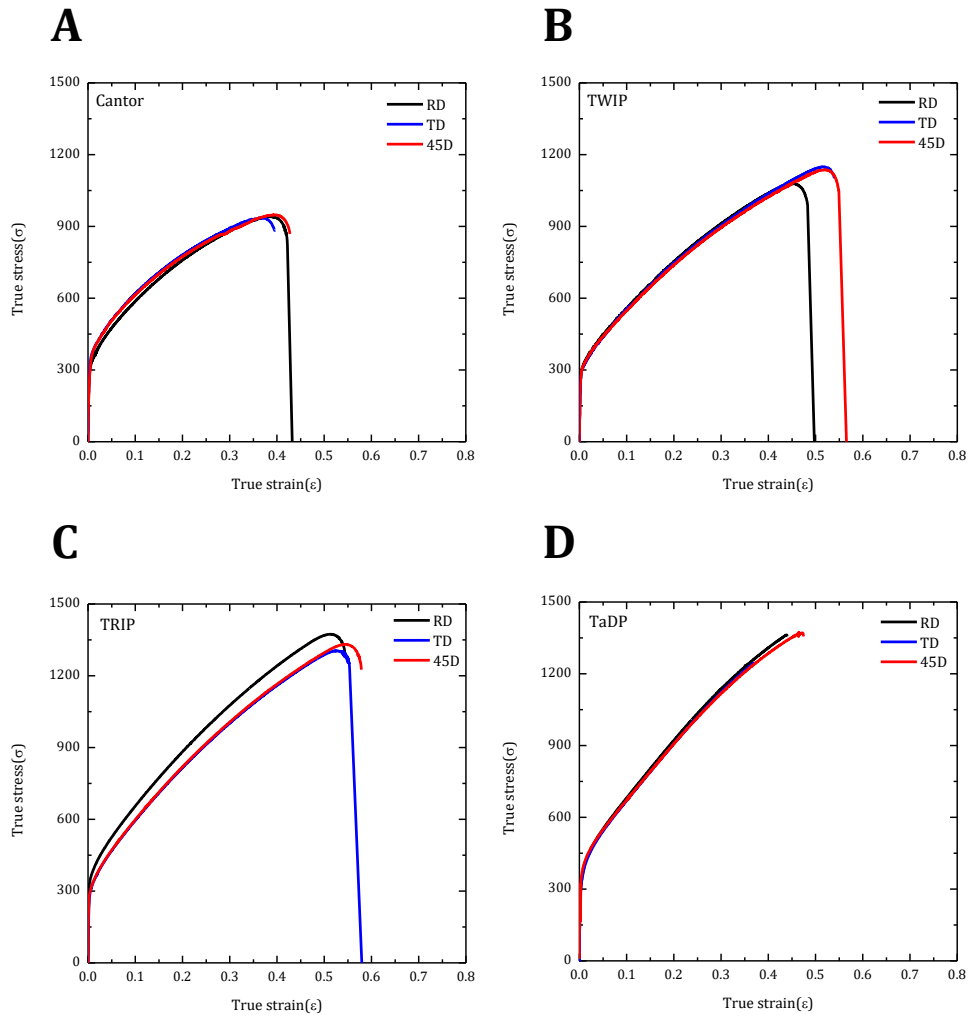


Figure 3.4. True stress stress strain curves along the three directions. (A) Cantor, (B) TWIP, (C) TRIP, and (D) TaDP CCAs.

Table 3.2. Mechanical properties of (A) Cantor, (B) TWIP, (C) TRIP, and (D) TaDP CCAs.

A

| Cantor | | | | | |
|---------------|----------------|------------------|-----------|--------------|-----------------|
| Direc. | Young' modulus | σ_y (MPa) | UTS (MPa) | ϵ_u | Possion's ratio |
| 0 | 181 | 307 | 679 | 0.37 | 0.25 |
| 45 | | 313 | 655 | 0.36 | |
| 90 | | 323 | 663 | 0.33 | |

B

| TWIP | | | | | |
|-------------|----------------|------------------|-----------|--------------|-----------------|
| Direc. | Young' modulus | σ_y (MPa) | UTS (MPa) | ϵ_u | Possion's ratio |
| 0 | 198 | 279 | 699 | 0.57 | 0.28 |
| 45 | | 273 | 685 | 0.56 | |
| 90 | | 273 | 689 | 0.52 | |

C

| TRIP | | | | | |
|-------------|----------------|------------------|-----------|--------------|-----------------|
| Direc. | Young' modulus | σ_y (MPa) | UTS (MPa) | ϵ_u | Possion's ratio |
| 0 | 188 | 288 | 798 | 0.6 | 0.31 |
| 45 | | 287 | 785 | 0.58 | |
| 90 | | 282 | 782 | 0.58 | |

D

| TaDP | | | | | |
|-------------|----------------|------------------|-----------|--------------|-----------------|
| Direc. | Young' modulus | σ_y (MPa) | UTS (MPa) | ϵ_u | Possion's ratio |
| 0 | 180 | 306 | 870 | 0.53 | 0.32 |
| 45 | | 305 | 785 | 0.53 | |
| 90 | | 305 | 782 | 0.53 | |

3.3.2. Anisotropy factor (R-value)

R value is powerful parameter to determine anisotropy of materials. R value is defined as ratio of width strain and thickness strain,

$$R = \frac{\varepsilon_w}{\varepsilon_t}. \quad \text{Eq. 3-3}$$

Where, ε_w is strain in the width direction, and ε_t is strain in the thickness direction. For an isotropic material R value is 1, and it affects the shape of yield surface.

Generally, average R value is used to determine shape of yield surface. Since R value is varying with rolling direction in the sheet specimen. The averaged R-value \bar{R} , is defined as,

$$\bar{R} = \frac{R_0 + R_{90} + 2R_{45}}{4}. \quad \text{Eq. 3-4}$$

Where, R_0 is R value for rolling direction, R_{90} is transverse direction from rolling direction, and R_{45} is R value for 45° off from rolling direction. Measured R-values are shown in Table 3.3.

Table 3.3. Comparison of anisotropy factor of each material.

| | Direction | Cantor | TWIP | TRIP | TaDP |
|---|------------------|---------------|-------------|-------------|-------------|
| R value | RD | 0.88 | 0.94 | 1.02 | 1.07 |
| | TD | 0.94 | 0.97 | 1.02 | 1.08 |
| | 45D | 1.02 | 0.97 | 1.03 | 1.07 |
| Anisotropy factor (\bar{R}) | | 0.86 | 0.96 | 1.01 | 1.09 |

3.4. Forming limit diagram prediction

3.4.1. Hardening law (Swift, Voce)

Stress strain curves obtained from the uniaxial tensile test exhibits only hardening behavior of uniform elongation region. Therefore, flow curves beyond ultimate tensile strength need to be fitted by hardening law. Swift and Voce hardening laws were used to determine hardening law suitable for the materials.

Swift hardening law [39] is described as,

$$\sigma = K(\bar{\epsilon}_p + e_0)^n, \quad \text{Eq. 3-5}$$

Voce hardening law [40] is described as,

$$\sigma = \sigma_0 + R(1 - e^{-b\bar{\epsilon}_p}), \quad \text{Eq. 3-6}$$

Figure 3.5 shows results of finite element (FE) analysis of load-displacement behavior depending on hardening law, and Table 3.4 shows fitting parameters. As shown in Figure 3.5, Voce hardening law matches better with experimental curve than the Swift hardening law. Therefore, FE analysis result with Voce hardening law was chosen for further analysis.

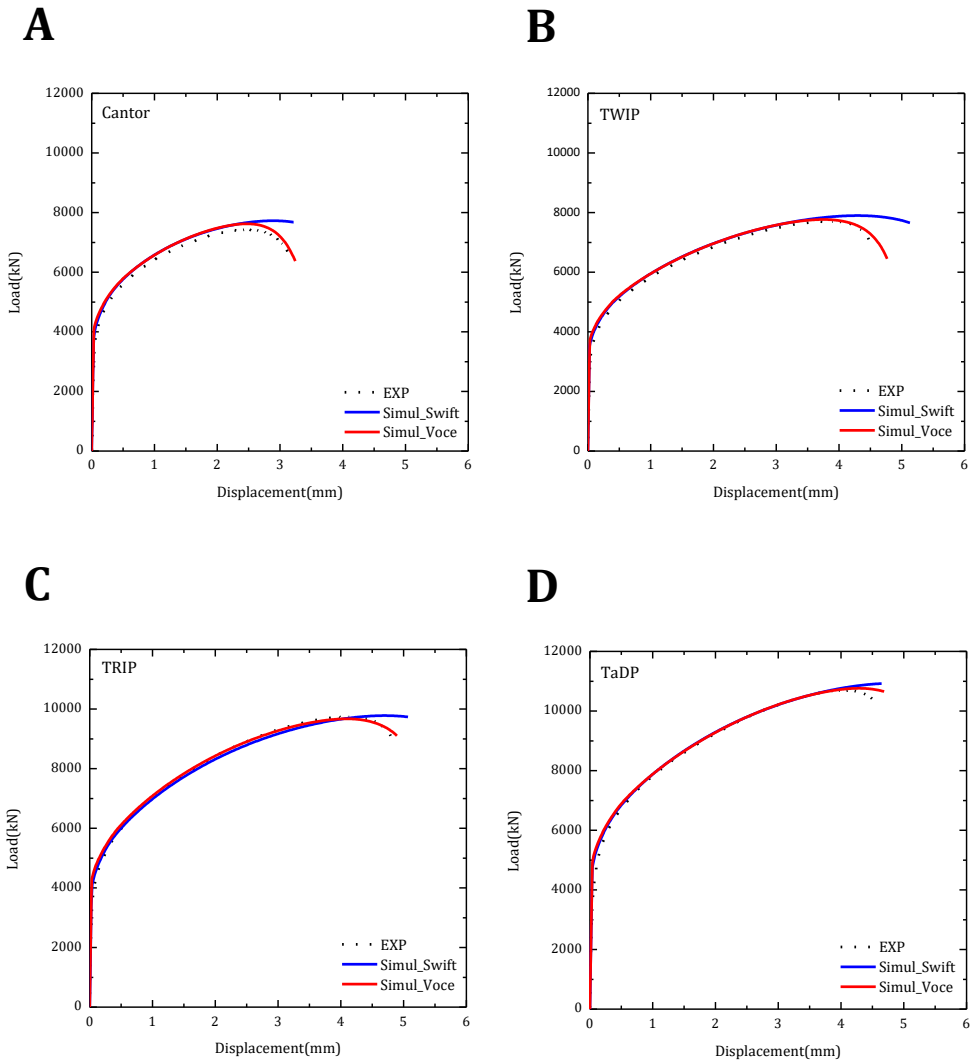


Figure 3.5. Comparison of Swift and Voce hardening law with experimental data. (A) Cantor, (B) TWIP, (C) TRIP, and (D) TaDP CCAs.

Table 3.4. Fitting parameters of hardening law. (A) Swift hardening law. (B) Voce hardening law.

A

| | K | e₀ | n |
|---------------|----------|----------------------|----------|
| Cantor | 1462.31 | 0.0261 | 0.4077 |
| TWIP | 1632.66 | 0.0471 | 0.5479 |
| TRIP | 1892.71 | 0.0445 | 0.5770 |
| TaDP | 2111.97 | 0.0564 | 0.6050 |

B

| | σ₀ | R | b |
|---------------|----------------------|----------|----------|
| Cantor | 355.67 | 793.36 | 4.1480 |
| TWIP | 322.91 | 1239.83 | 2.1954 |
| TRIP | 337.63 | 1587.39 | 1.9056 |
| TaDP | 387.86 | 1850.02 | 1.7314 |

3.4.2. Yield criteria (Mises, Hill 48, Yld 2000)

In this study, Hill's 1948 and Yield 2000-2d anisotropic plastic theories are employed to obtain effective stress for yielding occurs.

Hill's 1948 yield function [41] is expressed as,

$$F(\sigma_y - \sigma_z)^2 + G(\sigma_z - \sigma_x)^2 + H(\sigma_x - \sigma_y)^2 + 2L\tau_{yz}^2 + 2M\tau_{zx}^2 + 2N\tau_{xy}^2 = 1, \text{ Eq. 3-7}$$

Where, F, G, H, L, M, and N are anisotropic coefficients. For determination of anisotropic coefficients, yield stress from rolling (σ_y^{RD}) direction and r-value from three different rolling directions (R_0 , R_{45} , and R_{90}) were considered.

Yield 2000-2d yield function [42, 43] is expressed as,

$$f^\varphi = \bar{\sigma} = |\widetilde{S1}' - \widetilde{S11}'|^M + |\widetilde{S11}' - \widetilde{S1}'|^M + |2\widetilde{S1}'' - \widetilde{S11}''|^M. \text{ Eq. 3-8}$$

Where, $\bar{\sigma}$ is effective stress, M is exponent associated with crystal structure, and $\widetilde{S}k'$, $\widetilde{S}k''$ (k=1, 11) is modified deviatoric stress tensor. To identify Yield 2000-2d coefficients, yield stresses and r-value from three different rolling directions and biaxial tension data were considered. In this study, 8 is used for M value, due to face centered crystal structure, and biaxial tension data assumed as 1.

The yield surface of the Von Mises, Hill's 1948, and Yield 2000-2d for each sheet materials are shown in Figure 3.6. The input data are given in Table 3.5. The predicted results were matched well when the Yield 2000-2d yield criterion was used. Therefore, FE analysis result with Yield 2000-2d yield criterion was chosen for further analysis.

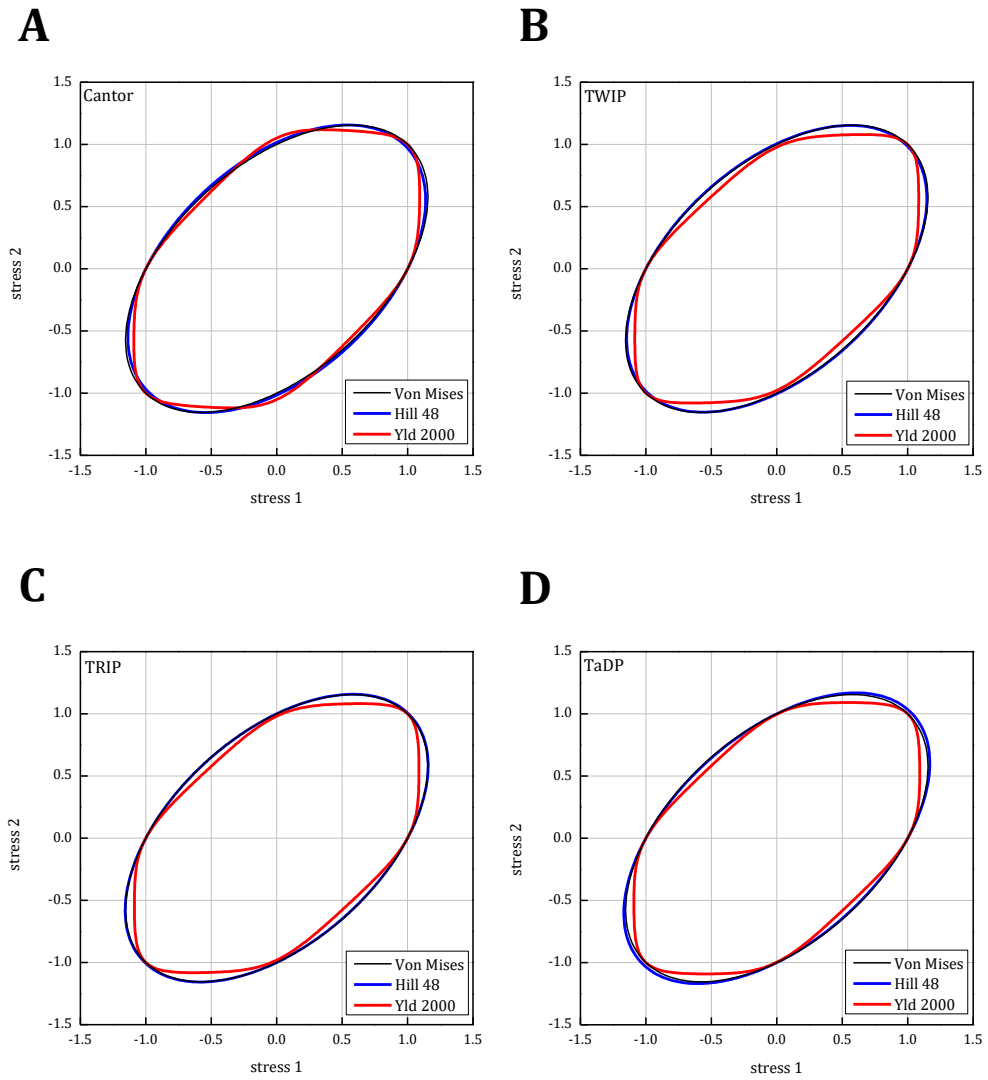


Figure 3.6. Yield surface of Von Mises, Hill’s 1948, and Yield 2000-2d. (A) Cantor, (B) TWIP, (C) TRIP, and (D) TaDP CCAs.

Table 3.5. The anisotropic coefficient for the
(A) Hill's 1948, and (B) Yield 2000-2d.

A

| | F | G | H | N |
|---------------|----------|----------|----------|----------|
| Cantor | 0.499199 | 0.531152 | 0.468848 | 1.567164 |
| TWIP | 0.50259 | 0.513242 | 0.486758 | 1.492663 |
| TRIP | 0.496486 | 0.496033 | 0.503967 | 1.516883 |
| TaDP | 0.48216 | 0.482835 | 0.517165 | 1.522569 |

B

| | A1 | A2 | A3 | A4 | A5 | A6 | A7 | A8 |
|---------------|-----------|-----------|-----------|-----------|-----------|-----------|-----------|-----------|
| Cantor | 1.04431 | 0.90059 | 1.06317 | 0.98111 | 0.99725 | 0.97849 | 0.98611 | 0.95688 |
| TWIP | 0.96485 | 1.04826 | 0.96956 | 1.01091 | 1.00490 | 0.99865 | 1.01469 | 1.05041 |
| TRIP | 0.97546 | 1.04397 | 0.97551 | 1.00801 | 1.00222 | 1.00385 | 1.00333 | 0.99960 |
| TaDP | 1.00095 | 1.01122 | 1.00164 | 0.9986 | 0.99793 | 1.00523 | 1.00751 | 0.99505 |

3.4.3. FLD prediction based on M-K model

To evaluate the formability of the CCAs, the construction of forming limit diagram (FLD) of Cantor, TWIP, TRIP, and TaDP CCAs were performed. The forming limit diagram (FLD) was simulated based on the material characterization.

The initial instability factor in the Marciniak and Kuczyski model (M-K model) was chosen to be 0.996. For the hardening behavior, Swift and Voce hardening laws were used to approximate the uniaxial stress strain curves. For the anisotropic yield function, Hill's 1948 and Yield 2000-2d were used to determine anisotropy yield surface (Figure 3.7).

The hardening law based on Swift hardening law overestimated the hardening behavior of CCAs. Therefore, Voce hardening law was considered to predict FLD. The anisotropic yield criteria based on Yield 2000-2d was used, due to Hill's 1948 overestimated the FLD. In conclusion, Voce hardening law combined with Yield 2000-2d yield criteria lead to best prediction of formability of CCAs (Figure 3.8). As expected from uniaxial tensile test, it showed good formability in the order of Cantor, TWIP, TRIP, and TaDP.

Figure 3.9 shows FLD of commercial alloys (Al6061-T6 [44], Ti6Al4V [44], 5083 Al-Mg [45], TRIP 700 [46], Fe15%MnAlC TWIP [46], EDDQ [46], IF [46], and Fe18%MnAlC TWIP [46]) with CCAs which is evaluated in this study. Al6061-T6, Ti6Al4V, and 5083 Al-Mg known for low formability materials, showed lower values than other alloys. Cantor, TWIP, TRIP, and TaDP CCAs showed almost similar value with commercial TRIP 700, EDDQ, and Fe15%MnAlC TWIP, and IF steel, respectively. However, there is no experimental data, additional investigations are necessary to improve responsibility.

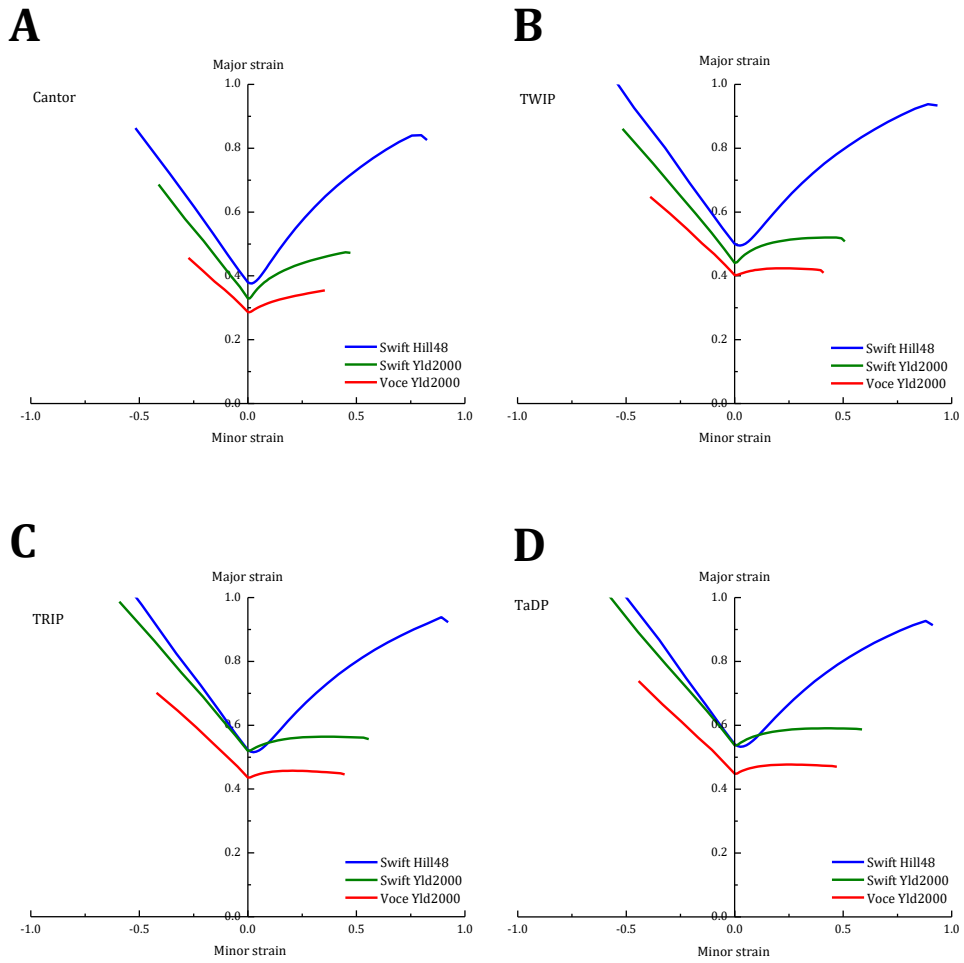


Figure 3.7. Comparison of forming limit diagram simulated by Marciniak-Kuczyski model with various material characterization. (A) Cantor, (B) TWIP, (C) TRIP, and (D) TaDP CCAs.

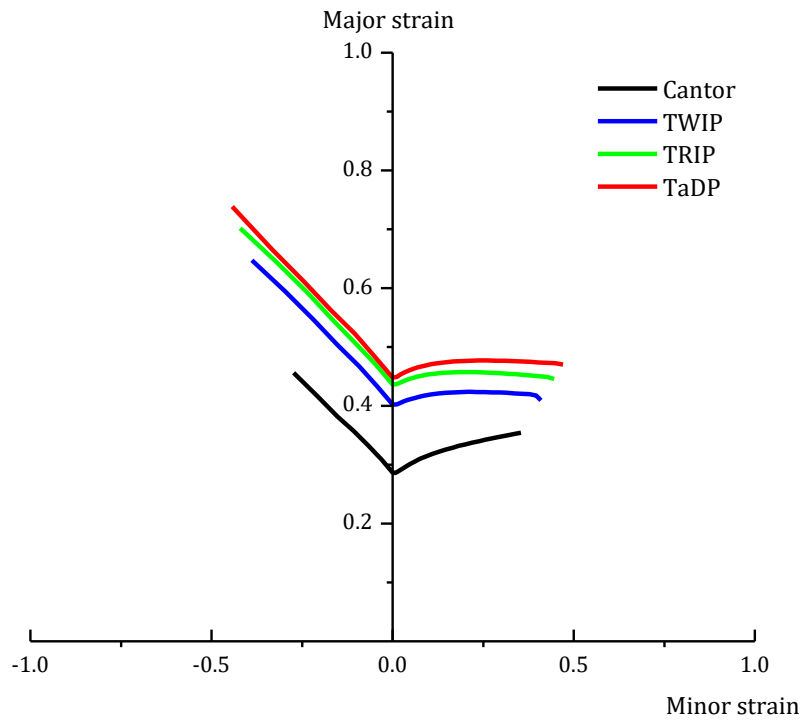


Figure 3.8. Determined forming limit diagram of Cantor, TWIP, TRIP, and TaDP CCAs.

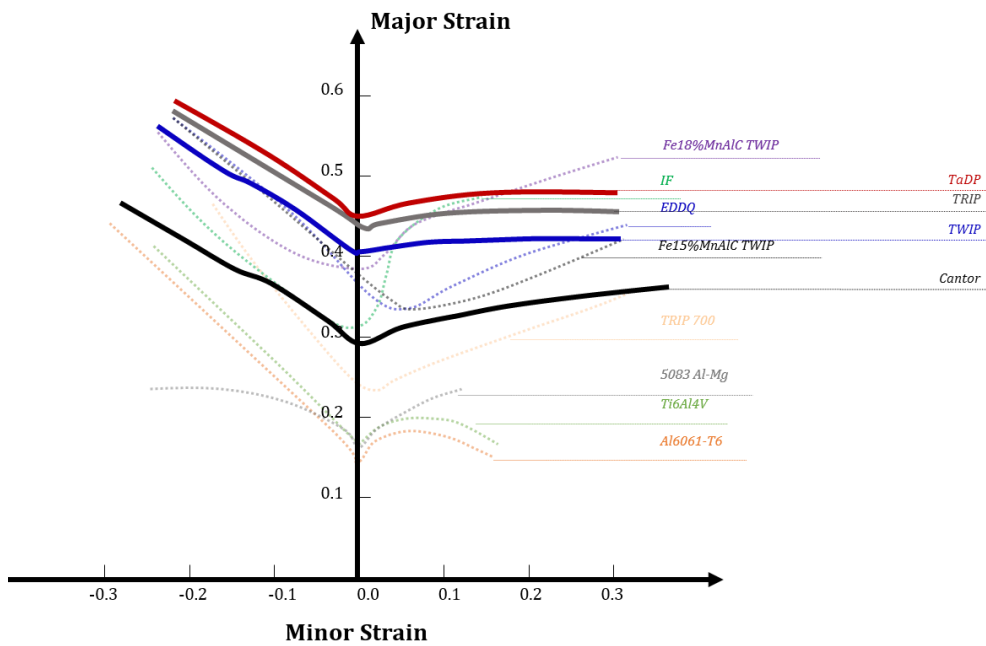


Figure 3.9. Comparison of forming limit diagram between commercial alloys and presented CCAs.

3.5. Limit dome height test

Stretch formability was evaluated in a limit dome height (LDH) testing machine using hemispherical punch. The diameter of hemispherical punch and punch speed were 20mm and 10^{-2} mm/sec, respectively. 55 x 55 mm² (length x width) rectangular specimen with 1.2~1.4mm thickness were used and silicone lubricant was used to minimize friction between punch and specimen. The LDH test was performed until a punch force decreased.

LDH test are performed on Cantor, TWIP, TRIP, and TaDP CCAs. Figure 3.10 exhibited photographs of deformed specimens. Punch force and displacement of punch are obtained from LDH test (Figure 3.11.).

The LDH value was obtained from the displacement value corresponding to the maximum punch load. LDH value is summarized in Table 3.6.

Punch displacement at fracture of Cantor, TWIP, TRIP, and TaDP are 8.195mm, 10.96mm, 9.68mm, and 7.98, respectively. As a result, in LDH test, CCAs with different deformation mechanisms showed good formability in the order of TWIP, TRIP, Cantor, and TaDP CCAs.

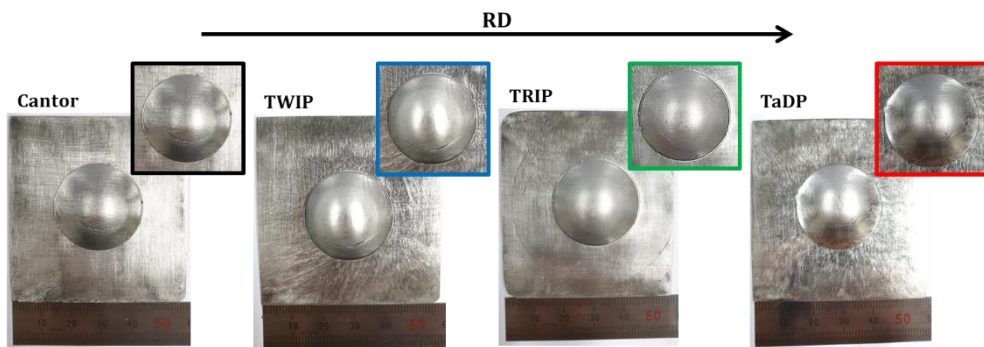


Figure 3.10. Photographs of the deformed CCAs: The enlarged photographs of each specimen showed fracture.

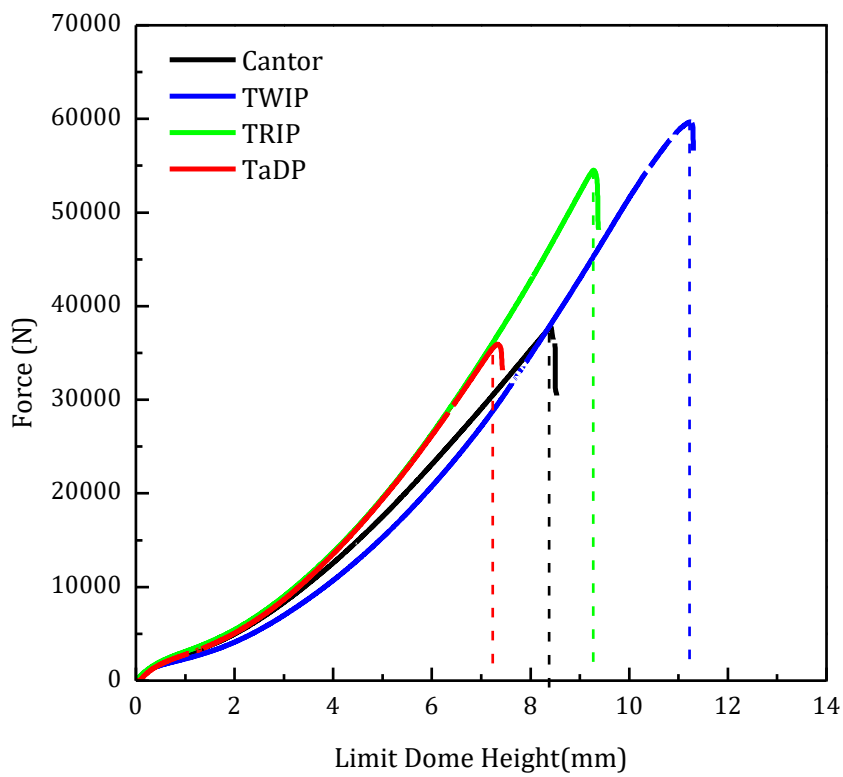


Figure 3.11. Force - limit dome height curves of Cantor, TWIP, TRIP, and TaDP CCAs during limit dome height test.

Table 3.6. Limit dome height value of Cantor, TWIP, TRIP, and TaDP CCAs.

| Notation | Limit Dome Height (mm) |
|-----------------|-------------------------------|
| Cantor | 8.195 |
| TWIP | 10.96 |
| TRIP | 9.68 |
| TaDP | 7.98 |

3.6. Trade-off between uniaxial stress state and biaxial stress state

In this study, evaluation of formability of complex concentrated alloys (CCAs) with different deformation mechanisms are carried out. Two methods, FLD and LDH, were used to evaluate formability.

Furthermore, FLD tendency of CCAs were compared with uniform elongation from uniaxial tensile test. As predicted from the uniaxial tensile test, it has good formability in order of Cantor, TWIP, TRIP, and TaDP CCAs. However, LDH value obtained in the LDH test exhibited different tendency from uniform elongation obtained in the uniaxial stress state.

Figure 3.12 illustrated different tendency in uniaxial and biaxial stress state. Blue and black solid lines represent the uniform elongation in uniaxial tensile test under uniaxial stress state and limit dome height in LDH test under biaxial stress state, respectively. In the case of materials deformed by phase transformation, such as TRIP and TaDP, plastic flow decreases in forming process.

The tendency shown in Figure 3.12 could be explained for two reasons. The first is that uniform elongation obtained from uniaxial tensile test contains only information up to strain localization, while LDH obtained from biaxial stress state contains not only strain localization but also information up to fracture. Secondly, since the real forming process includes not only uniaxial stress state but also multiaxial stress state and shear stress. Thus, further study is necessary for a deeper understanding of microstructure evolution under various stress state condition. Therefore, in the following section, the effects of the microstructure evolution under various stress state are presented.

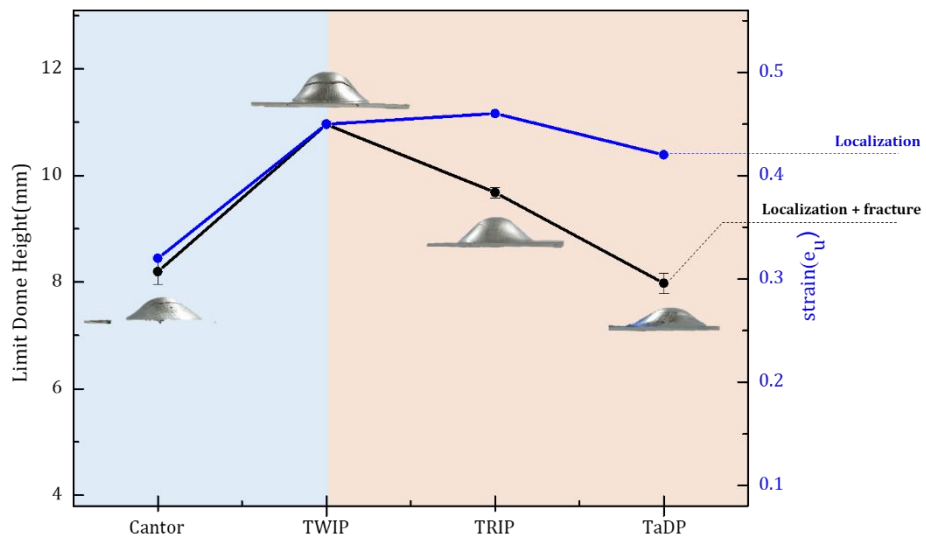


Figure 3.12. Blue and black solid lines represent the uniform elongation in uniaxial tensile test under uniaxial stress state and limit dome height in LDH test under biaxial stress state, respectively.

Chapter 4. Effect of stress state on formability

Fracture test was performed to analyze the effect of stress states on formability under various deformations mechanisms. Therefore, a central hole test was performed to represent the uniaxial stress state. In addition, the notched test was conducted to have plane stress state that is known to be widely applied in the real forming process.

The fracture specimen of central hole test after fracture is shown in Figure 4.1A. According to FE simulation, deformed area next to the hole could be confirmed nearly uniaxial strain condition as shown in Figure 4.2 A.

The fracture specimen of notched test after fracture is shown in Figure 4.1B. According to FE simulation, the center of deformed area could be confirmed nearly plane strain condition as shown in Figure 4.2 B.

In the case of Cantor CCA deformed through dislocation gliding during deformation, the equivalent strain at the onset of fracture increases in the plane strain condition compared to the uniaxial strain condition. For the TWIP CCA deformed through twinning during deformation, the equivalent strain at the onset of fracture increases in the plane strain condition compared to the uniaxial strain condition. However, for the TRIP and TaDP CCAs deformed through phase transformation during deformation, the equivalent strain at the onset of fracture decreases in the plane strain condition than in the uniaxial strain condition (Figure 4.2).

Therefore, in this chapter, investigation of deformation behavior tendency by microstructure evolution under various strain condition are presented.

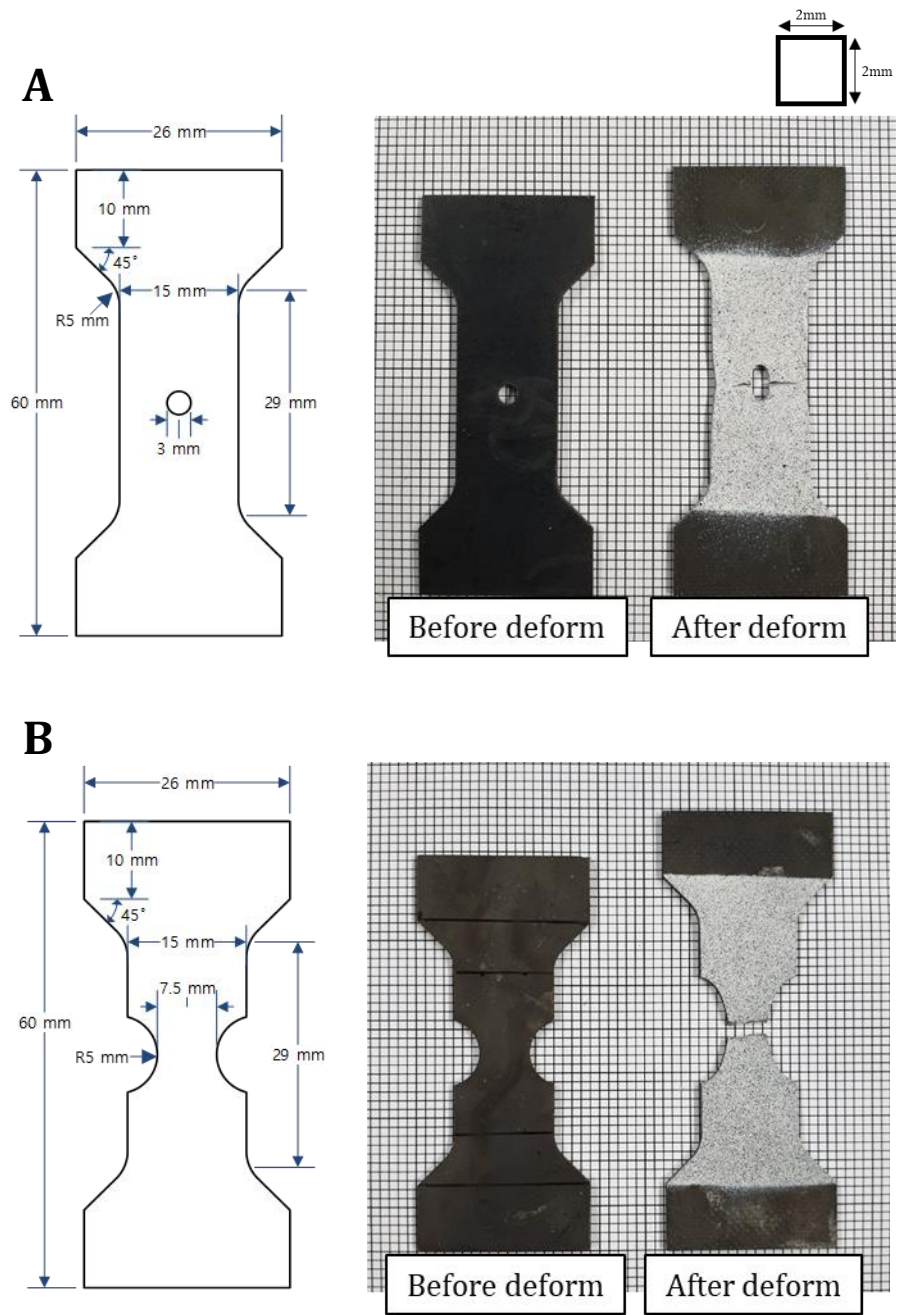


Figure 4.1. Fracture specimen after fracture. (A) Central hole test. (B) Notched test.

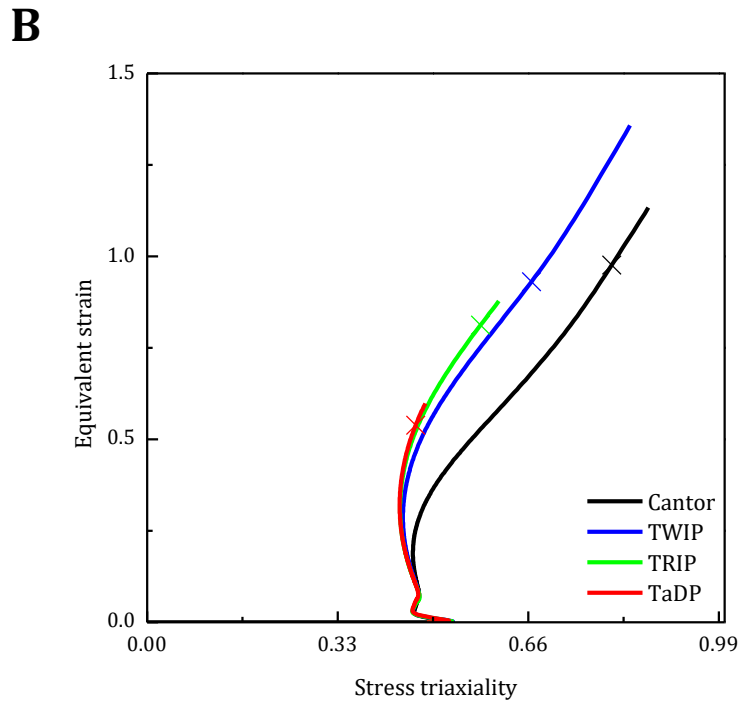
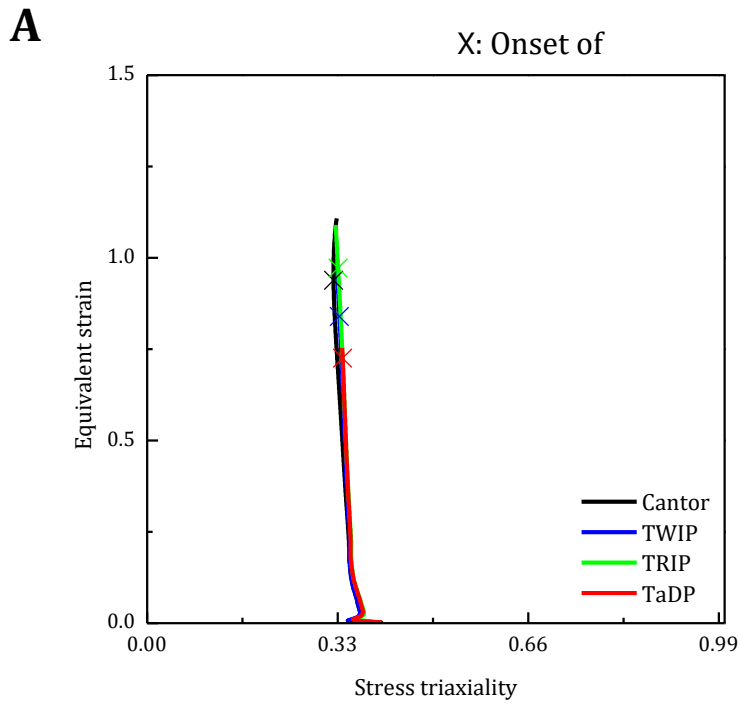


Figure 4.2. Relation of stress triaxiality and equivalent strain of (A) Central hole test, and (B) Notched test.

4.1. Effect of stress state on deformation behavior of TWIP complex concentrated alloy

4.1.1. Equivalent strain and stress history

The results of TWIP CCA from digital image correlation (DIC) and FE analysis in form of equivalent strain and triaxiality (η) are shown in Figure 4.3. Triaxiality is stress state parameter. The x marks in the Figure 4.3 represents the point of onset of fracture determined in the fracture test.

The central hole test of TWIP CCA exhibits that stress triaxiality is almost constant at 0.33 during deformation. In this case the triaxiality of 0.33 represents that it is uniaxial strain condition during deformation. The notched test of TWIP CCA exhibits that stress triaxiality is not constant during deformation. It changes from plane strain condition to biaxial strain condition during deformation. In conclusion, from the FE simulation, stress triaxiality is expressed as a function of equivalent plastic strain.

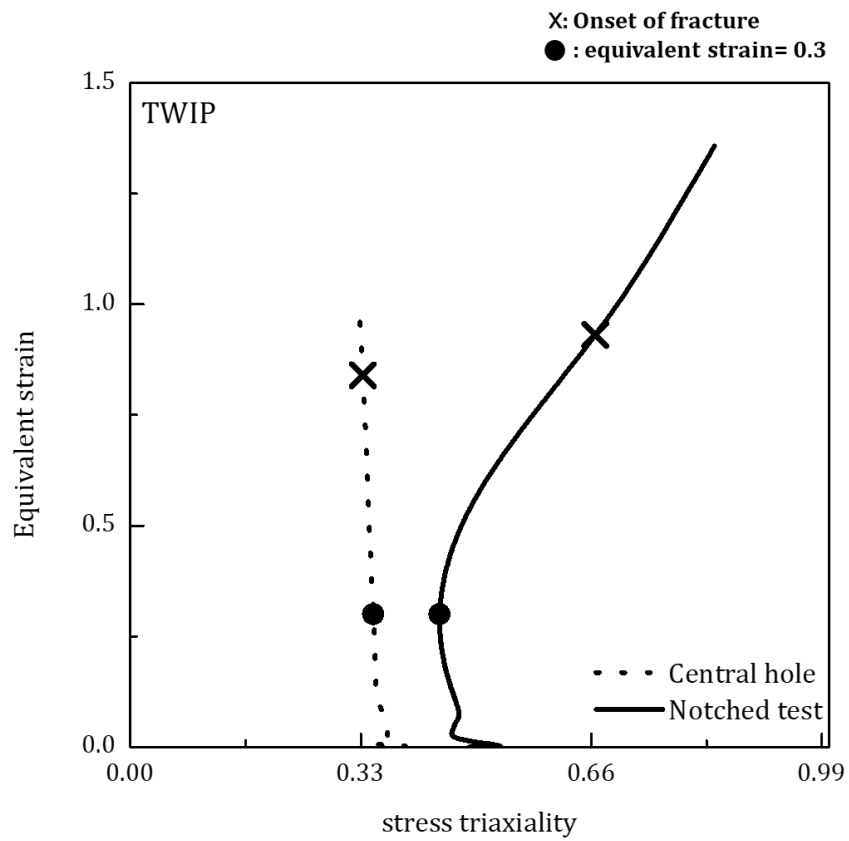


Figure 4.3. Relation of stress triaxiality and equivalent strain of TWIP CCA.

4.1.2. Comparison of twinning thickness under different stress state by using ECCI analysis

In order to understand the deformation behavior under various stress state, it is necessary to compare the microstructure at same equivalent strain. Thus, fracture tests were interrupted at same equivalent strain ($\epsilon_{eq} = 0.3$) in the central hole test and notched test. The FE simulations showed that the equivalent strain is 0.3 at the displacements of 1.346 mm and 3.508 mm in the central hole test and notched test, respectively. The circle marks in Figure 4.3 indicates when the equivalent strain is 0.3.

From the above results, the fracture test was interrupted when the displacements were 1.346 mm and 3.508 mm in the central hole test and notched test, respectively. Figure. 4.4 is load displacement curve up to equivalent strain of 0.3 for TWIP CCA. Central hole test was indicated by the dotted line and notched test was indicated by solid line.

In the case of Fe-Mn-C TWIP steels [47], there is a difference in the twinning thickness as a function of stress state, which causes a large difference in the mechanical properties. Therefore, microstructures were compared between the uniaxial strain and plane strain condition.

Figure. 4.5A presents electron channeling contrast imaging (ECCI) microstructure of a central hole specimen deformed in uniaxial strain condition at equivalent strain = 0.3. In Figure. 4.5A, the twinning thickness in 1 and 2 areas were measured, and the thickness was $2.139\mu\text{m} \pm 1\mu\text{m}$. Figure. 4.5B presents ECCI microstructure of a notched specimen deformed in plane strain condition at

equivalent strain = 0.3. In Figure. 4.5B, the twinning thickness in 1 and 2 areas were measured, and the thickness was $2.03\mu\text{m} \pm 0.73\mu\text{m}$.

The above results show that CCA with deformation mechanism of twinning has a constant twinning thickness regardless of the strain condition. Therefore, in the case of TWIP CCA, the tendency of uniform elongation obtained from uniaxial tensile test and limit dome height value obtained from limit dome height test were similar.

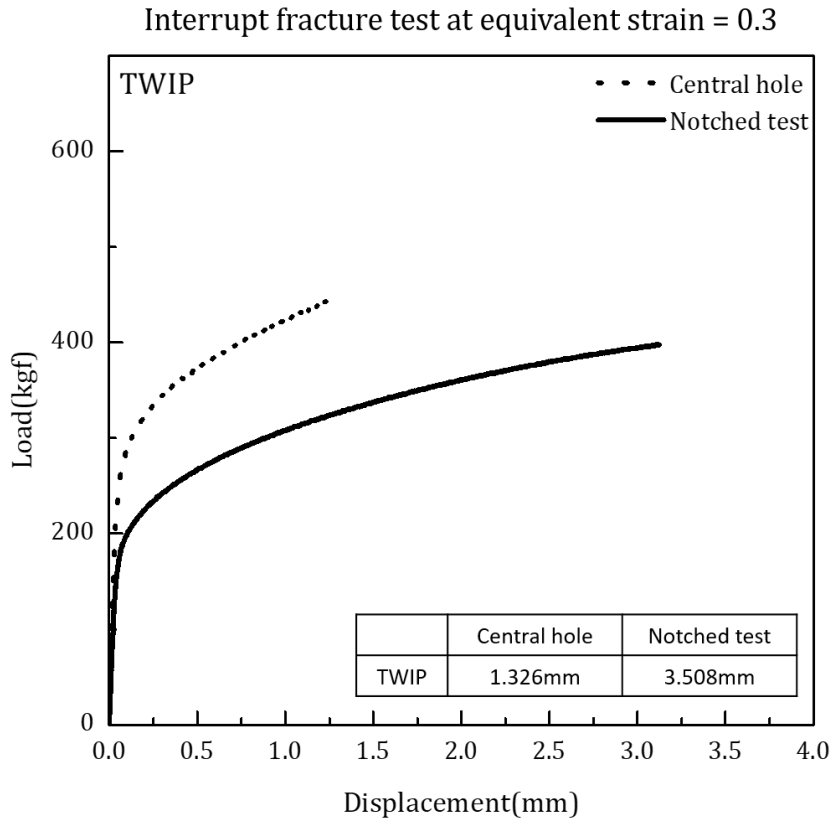


Figure 4.4. TWIP CCA is deformed respectively by central hole and notched test up to the same level of equivalent strain = 0.3.

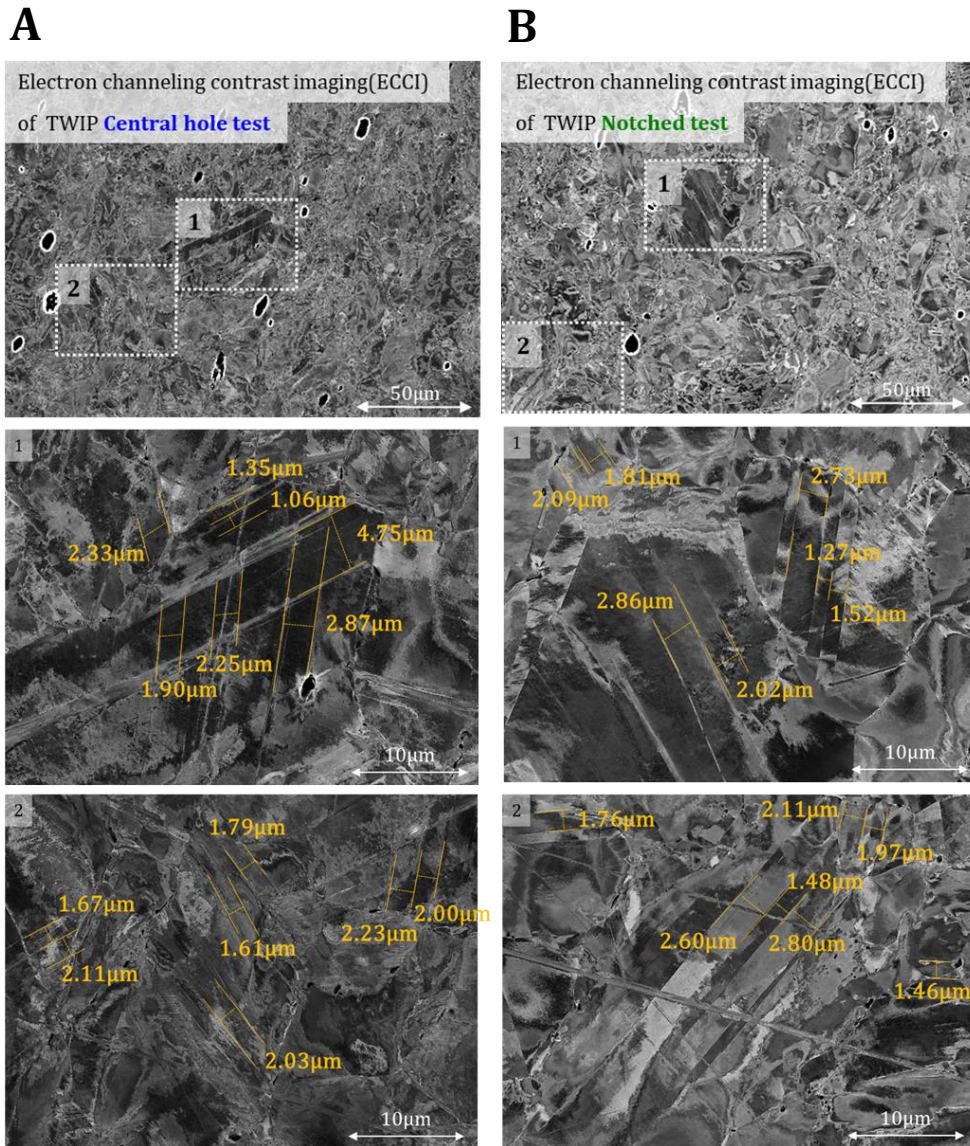


Figure 4.5. Electron channeling contrast image (ECCI) of TWIP CCA by (A) central hole and (B) notched test up to level of equivalent strain = 0.3, revealing thickness of twin is independent by stress state.

4.2. Effect of stress state on deformation behavior of TRIP complex concentrated alloy

4.2.1. Equivalent strain and stress history

The results of TRIP CCA from digital image correlation (DIC) and FE analysis in form of equivalent strain and triaxiality (η) are shown in Figure 4.6. Triaxiality is stress state parameter. The x marks in the Figure 4.6 represents the point of onset of fracture determined in the fracture test.

The central hole test of TRIP CCA exhibits that stress triaxiality is almost constant at 0.33 during deformation. In this case the triaxiality of 0.33 represents that it is uniaxial strain condition during deformation. The notched test of TRIP CCA exhibits that stress triaxiality is not constant during deformation. It changes from plane strain condition to biaxial strain condition during deformation. In conclusion, from the FE simulation, stress triaxiality is expressed as a function of equivalent plastic strain.

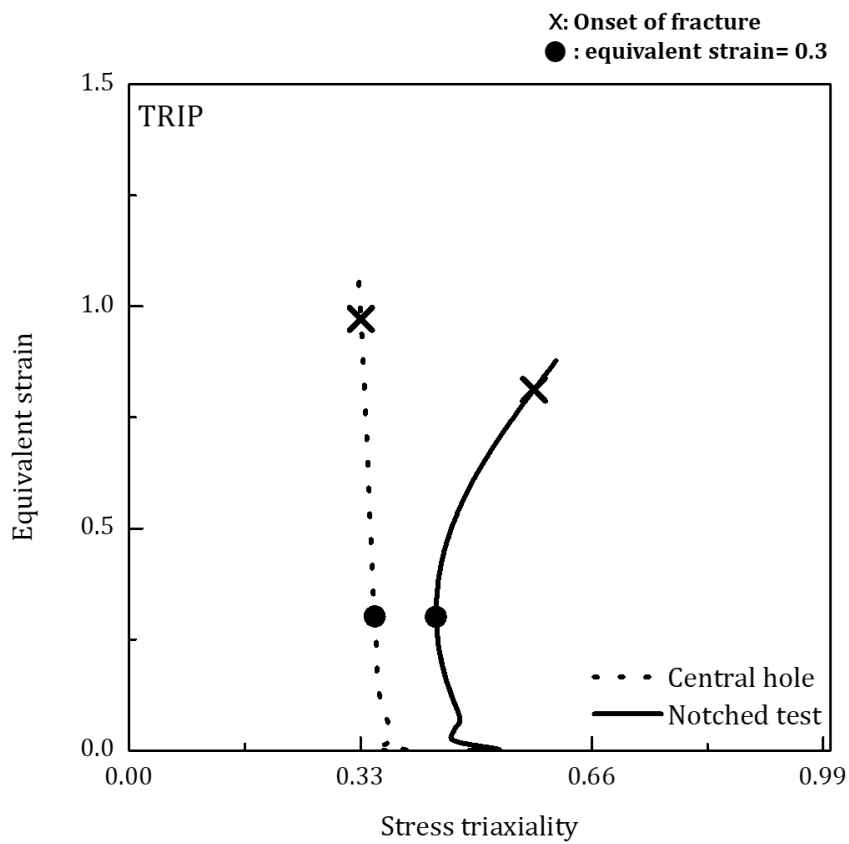


Figure 4.6. Relation of stress triaxiality and equivalent strain of TRIP CCA.

4.2.2. Comparison of phase transformation under different stress state by using EBSD analysis

In order to understand the deformation behavior according to stress state, microstructure analysis was conducted through Electron backscatter diffraction (EBSD) at same equivalent strain. The fracture tests were interrupted at same equivalent strain ($\epsilon_{eq} = 0.3$) in the central hole test and notched test. The FE simulations showed that the equivalent strain is 0.3 at the displacements of 1.388 mm and 3.565 mm in the central hole test and notched test, respectively. The circle marks in Figure 4.6 indicates when the equivalent strain is 0.3.

From the above results, fracture test was interrupted when the displacements were 1.388 mm and 3.565 mm in the central hole test and notched test, respectively. Figure. 4.7 is load displacement curve up to equivalent strain of 0.3 for TRIP CCA. Central hole test was indicated by the dotted line and notched test was indicated by solid line.

In the case of Transformation Induced Plasticity (TRIP) steels [48], martensite transformation occurs as secondary deformation mechanism. This deformation mechanism bringing large enhancement of plastic flow, due to postpones the onset of necking.

Figure. 4.8A presents EBSD phase map of a central hole specimen deformed in uniaxial strain condition up to equivalent strain = 0.3. Phase fraction of austenite and martensite were 67% and 33%, respectively. Figure. 4.8B presents EBSD phase map of a notched specimen deformed in plane strain condition to equivalent strain = 0.3. Phase fraction of austenite and martensite were 80% and 20%, respectively.

Revealing clear difference in phase transformation tendency as a function of strain condition.

The above results show that CCA with phase transformation occurred more easily in uniaxial strain condition. Thus, more additional plastic flow occurs in uniaxial strain condition than in plane strain condition.

Therefore, in the case of TRIP CCA, limit dome height value obtained from the limit dome height test decreased compared to uniform elongation obtained from the uniaxial tensile test.

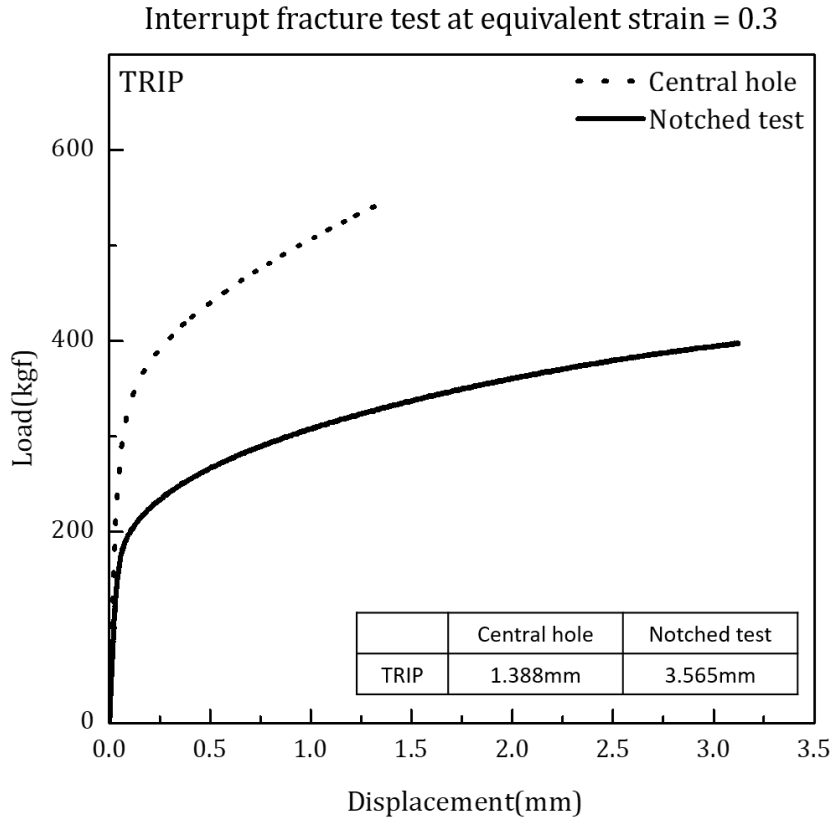
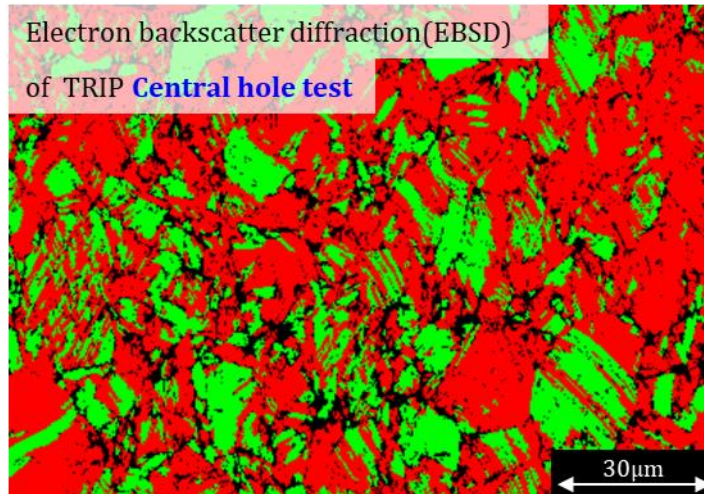


Figure 4.7. TRIP CCA is deformed respectively by central hole and notched test up to the same level of equivalent strain = 0.3.

A



B

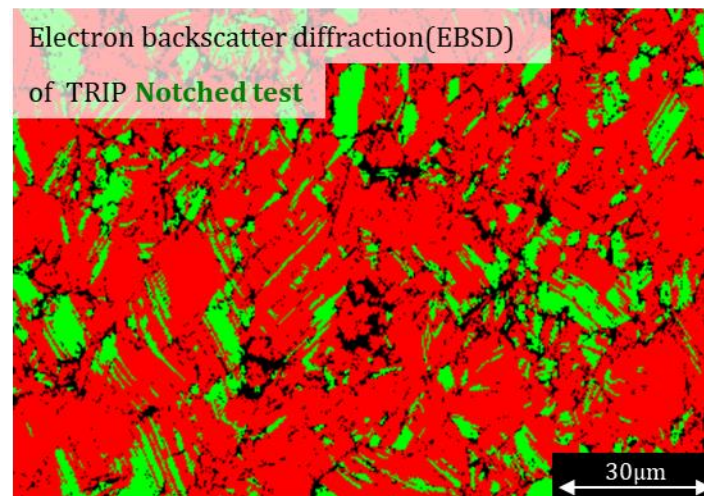


Figure 4.8. Electron backscatter diffraction (EBSD) of TRIP CCA by (A) central hole and (B) notched test up to level of equivalent strain = 0.3.

4.3. Effect of stress state on deformation behavior of TaDP complex concentrated alloy

4.3.1. Equivalent strain and stress history

The results of TaDP CCA from digital image correlation (DIC) and FE analysis in form of equivalent strain and triaxiality (η) are shown in Figure 4.6. Triaxiality is stress state parameter. The x marks in the Figure 4.9 represents the point of onset of fracture determined in the fracture test.

The central hole test of TRIP CCA exhibits that stress triaxiality is almost constant at 0.33 during deformation. In this case the triaxiality of 0.33 represents that it is uniaxial strain condition during deformation. The notched test of TaDP CCA exhibits that stress triaxiality is not constant during deformation. It changes from plane strain condition to biaxial strain condition during deformation. In conclusion, from the FE simulation, stress triaxiality is expressed as a function of equivalent plastic strain.

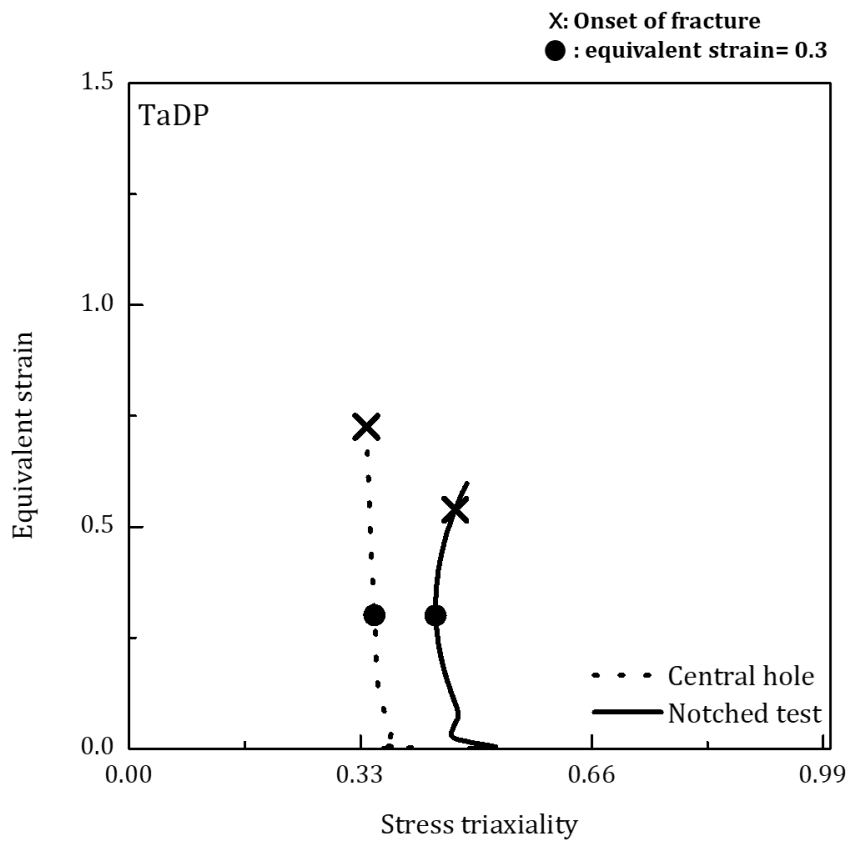


Figure 4.9. Relation of stress triaxiality and equivalent strain of TaDP CCA.

4.3.2. Comparison of phase transformation under different stress state by using EBSD analysis

In order to understand the deformation behavior according to stress state, microstructure analysis was conducted through Electron backscatter diffraction (EBSD) at same equivalent strain. The fracture tests were interrupted at same equivalent strain ($\epsilon_{eq} = 0.3$) in the central hole test and notched test. The FE simulations showed that the equivalent strain is 0.3 at the displacements of 1.268 mm and 3.113 mm in the central hole test and notched test, respectively. The circle marks in Figure 4.9 indicates when the equivalent strain is 0.3.

Therefore, the fracture test was interrupted when the displacements were 1.268 mm and 3.113 mm in the central hole test and notched test, respectively. Figure. 4.10 is load displacement curve up to equivalent strain of 0.3 for TaDP CCA. Central hole test was indicated by the dotted line and notched test was indicated by solid line.

In the case of Transformation Induced Plasticity steels [48], martensite transformation occurs as secondary deformation mechanism. This deformation mechanism bringing large enhancement of plastic flow, due to postpones the onset of necking.

Figure. 4.11A presents EBSD phase map of a central hole specimen deformed in uniaxial strain condition up to equivalent strain = 0.3. Phase fraction of austenite and martensite were 39.7% and 60.3%, respectively. Figure. 4.11B presents EBSD phase map of a notched specimen deformed in plane strain condition to equivalent strain = 0.3. Phase fraction of austenite and martensite were 45.5% and 54.5%, respectively. Revealing clear difference in phase transformation tendency as a

function of strain condition.

The above results show that CCA with phase transformation occurred more easily in uniaxial strain condition. Thus, more additional plastic flow occurs in uniaxial strain condition than in plane strain condition.

Therefore, in the case of TaDP CCA, limit dome height value obtained from the limit dome height test decreased compared to uniform elongation obtained from the uniaxial tensile test.

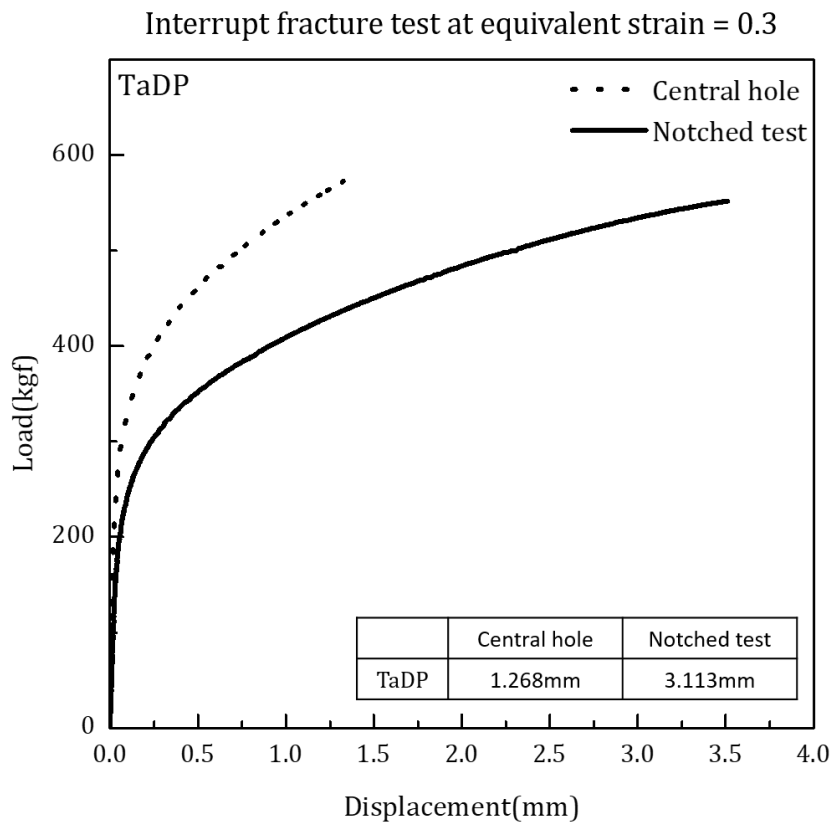
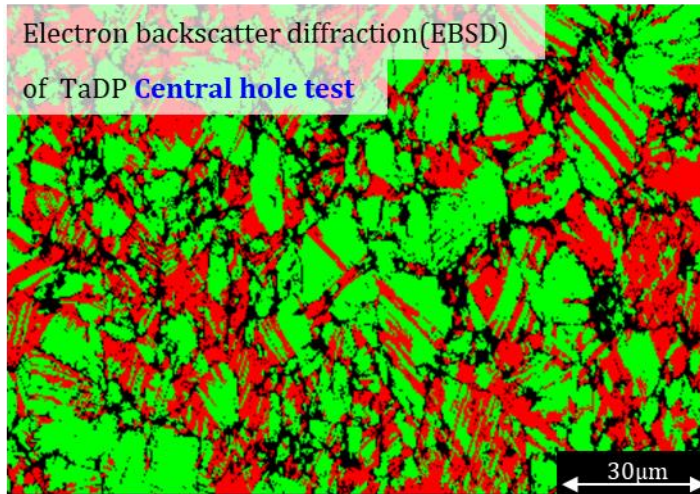


Figure 4.10. TaDP CCA is deformed respectively by central hole and notched test up to the same level of equivalent strain = 0.3.

A



B

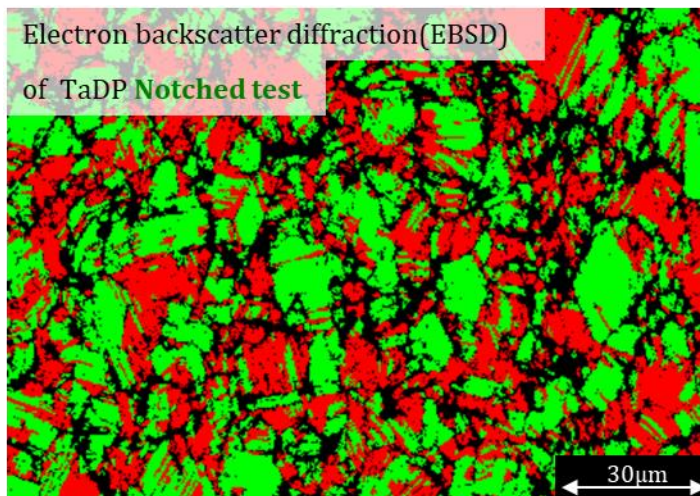


Figure 4.11. Electron backscatter diffraction (EBSD) of TaDP CCA by (A) central hole and (B) notched test up to level of equivalent strain = 0.3.

4.4. Comparison of deformation behavior under various stress state

In this study, comparison of deformation behavior under various stress state are carried out to understand microstructure evolution under various strain condition. Generally, it is well known that plane strain condition is frequently occurred during forming. Thus, in order to understand the forming characteristic of the materials, the microstructure analysis under plane strain condition was conducted.

Therefore, in this chapter, the central hole test which represents the stress state of uniaxial tensile test, and the notched test which represents the stress state of the limit dome height were performed. Central hole test indicates uniaxial strain condition at deformed area next to the hole, and notched test indicate plane strain condition at center of deformed area. To compare microstructure evolution in the central hole test and notched test, fracture test was interrupted at same equivalent strain (= 0.3) level.

Electron channeling contrast image (ECCI) analysis was conducted to compare difference of twinning thickness according to stress state in TWIP CCA. TWIP CCA exhibited constant twinning thickness regardless of the strain condition. Therefore, the tendency of uniform elongation obtained from uniaxial tensile test and limit dome height value obtained from limit dome height test were similar.

For the phase transformation materials such as TRIP and TaDP, Electron backscatter diffraction (EBSD) analysis was conducted to compare difference of phase transformation tendency according to stress state. Comparing the phase maps, phase transformation occurred more easily in uniaxial strain condition. Thus, more

additional plastic flow occurs in uniaxial strain condition than in plane strain condition. Therefore, in the case of TaDP CCA, limit dome height value obtained from the limit dome height test decreased compared to uniform elongation obtained from the uniaxial tensile test.

Chapter 5. Conclusion

In this study, the effect of deformation mechanism on the formability of complex concentrated alloys (CCAs) are systematically evaluated. Herein, to demonstrate the effect of deformation mechanism on the formability of CCAs, stacking fault energy (SFE) was varied. After that forming limit diagram (FLD) and limit dome height (LDH) test are carefully constructed by numerical simulations and experiments, respectively.

In the uniaxial tensile test, the CCAs were predicted to show good formability in order of Cantor, TWIP, TRIP, and TaDP CCAs. The FLD results showed good match with the above prediction. However, the LDH values from the LDH test didn't match with uniaxial tensile test tendency. Against the uniaxial tensile test, LDH value of TRIP and TaDP CCAs which deformed by phase transformation were significantly below values of the uniform elongation. Therefore, microstructure analysis under various stress state are performed to understand above phenomenon.

Central hole specimen is designed to obtain uniaxial strain condition that represent the strain condition of uniaxial tensile test. Notched specimen is designed to obtain plane strain condition that represent strain condition of forming process.

For the twinning induced material such as TWIP CCA, ECCI analysis was conducted to compare difference of twinning thickness. TWIP CCA exhibited constant twinning thickness regardless of the strain condition. Therefore, the tendency of uniform elongation obtained from uniaxial tensile test and limit dome height from value obtained from limit dome height test were similar.

For the phase transformation materials such as TRIP and TaDP, EBSD analysis

was conducted to compare phase transformation tendency for various stress state. Comparing the phase maps, phase transformation occurred more easily in uniaxial strain condition. This results in additional plastic flow under uniaxial strain condition rather than plane strain condition. Therefore, the early stage of failure occurred during limit dome height test compared to uniaxial tensile test.

In order to find the CCA composition with optimized formability, the study was also conducted on the composition between Cantor and TWIP, and between TWIP and TRIP. New composition of CCAs are presented in Table 5.1. Notation was determined according to Mn contents (CCA19 ~ CCA11).

As shown in Figure 5.1, Uniaxial tensile test was performed to compare uniform elongation. After that microstructure analysis was performed to identify deformation mechanism of each material. Figure 5.2 is microstructure of onset of fracture region. CCA19 and CCA18 showed dislocation gliding as deformation mechanism. CCA 17 to CCA13 showed twinning as deformation mechanism. CCA 12 and CCA 11 showed phase transformation as deformation mechanism.

Figure 5.3 exhibited the uniform elongation of Cantor, TWIP, TRIP, TaDP CCAs and newly designed CCAs. Also Figure 5.3 shows that CCA 15 to CCA 11 had a high uniform elongation compared with other CCAs. Alloys in the blue, green, and orange regions are deformed through dislocation gliding, twinning, and phase transformation, respectively.

From the above results, CCA 15 to CCA11 showed high uniform elongation, and among them CCA 15, TWIP CCA, and CCA 13 showed twinning deformation mechanism. Therefore, CCA15, TWIP CCA, and CCA13 are expected to have good formability in FCC CCAs system.

Table 5.1. Composition of new designed CCAs.

| # | Note | Composition | Deformation mechanism |
|---|--------|--|-----------------------|
| - | Cantor | $\text{Cr}_{20}\text{Mn}_{20}\text{Fe}_{20}\text{Co}_{20}\text{Ni}_{20}$ | Dislocation gliding |
| 1 | CCA19 | $\text{Cr}_{20}\text{Mn}_{19}\text{Fe}_{21}\text{Co}_{21}\text{Ni}_{19}$ | |
| 2 | CCA18 | $\text{Cr}_{20}\text{Mn}_{18}\text{Fe}_{22}\text{Co}_{22}\text{Ni}_{18}$ | |
| 3 | CCA17 | $\text{Cr}_{20}\text{Mn}_{17}\text{Fe}_{23}\text{Co}_{23}\text{Ni}_{17}$ | |
| 4 | CCA16 | $\text{Cr}_{20}\text{Mn}_{16}\text{Fe}_{24}\text{Co}_{24}\text{Ni}_{16}$ | |
| 5 | CCA15 | $\text{Cr}_{20}\text{Mn}_{15}\text{Fe}_{25}\text{Co}_{25}\text{Ni}_{15}$ | |
| - | TWIP | $\text{Cr}_{20}\text{Mn}_{14}\text{Fe}_{26}\text{Co}_{26}\text{Ni}_{14}$ | Twinning |
| 6 | CCA13 | $\text{Cr}_{20}\text{Mn}_{13}\text{Fe}_{27}\text{Co}_{27}\text{Ni}_{13}$ | |
| 7 | CCA12 | $\text{Cr}_{20}\text{Mn}_{12}\text{Fe}_{28}\text{Co}_{28}\text{Ni}_{12}$ | |
| 8 | CCA11 | $\text{Cr}_{20}\text{Mn}_{11}\text{Fe}_{29}\text{Co}_{29}\text{Ni}_{11}$ | |
| - | TRIP | $\text{Cr}_{20}\text{Mn}_{10}\text{Fe}_{30}\text{Co}_{30}\text{Ni}_{10}$ | Phase transformation |
| - | TaDP | $\text{Cr}_{20}\text{Mn}_8\text{Fe}_{32}\text{Co}_{32}\text{Ni}_8$ | Phase transformation |

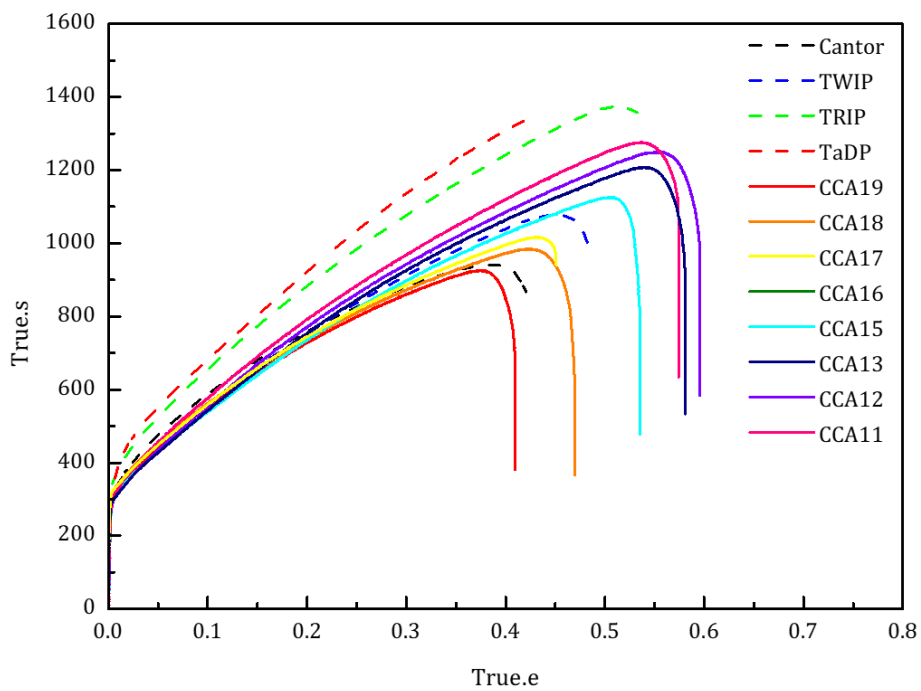
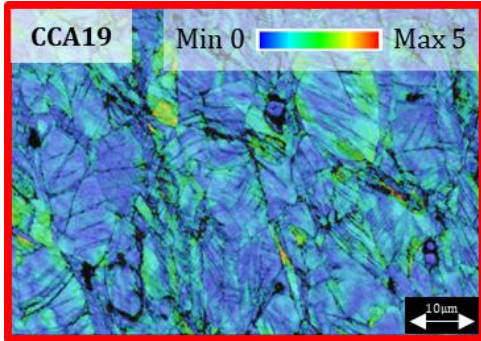
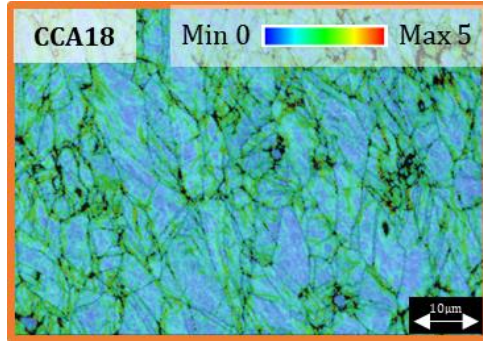


Figure 5.1. Tensile behavior of new CCAs system compared to Cantor, TWIP, TRIP, and TaDP CCAs.

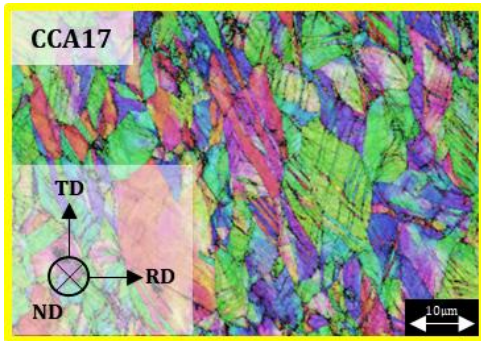
A



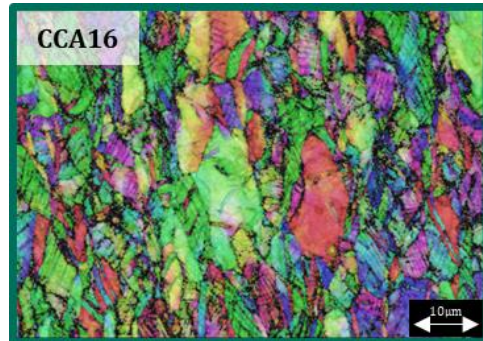
B



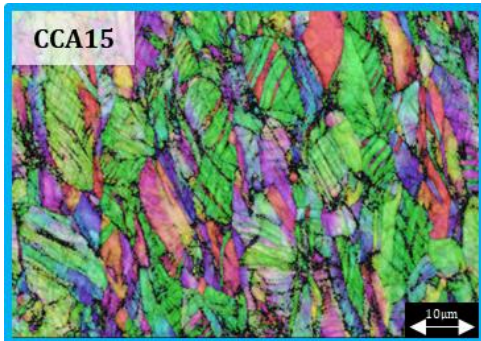
C



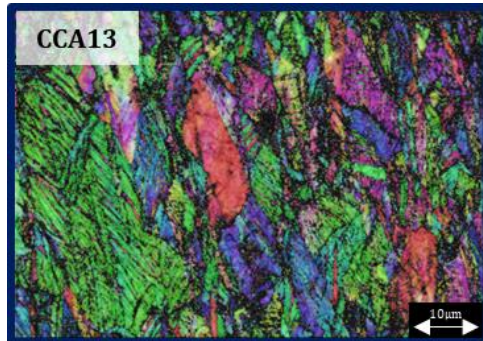
D



E



F



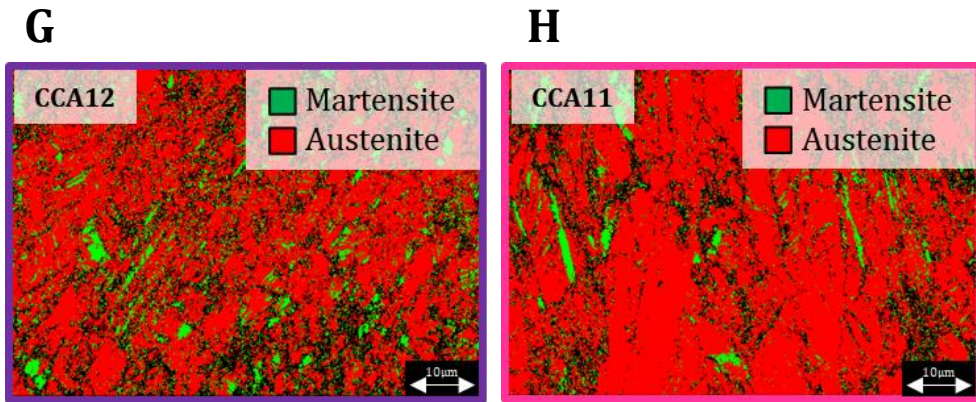


Figure 5.2. EBSD maps of new CCAs system. (A) The main deformation mechanism of CCA19 is the dislocation glide as shown in KAM maps. (B) The main deformation mechanisms of CCA18 is the dislocation glide as shown in KAM maps. (C) The main deformation mechanisms of CCA17 is twinning as shown in IPF maps. (D) The main deformation mechanisms of CCA16 is twinning as shown in IPF maps. (E) The main deformation mechanisms of CCA15 is twinning as shown in IPF maps. (F) The main deformation mechanisms of CCA13 is twinning as shown in IPF maps. (G) The main deformation mechanisms of CCA12 is phase transformation as shown in phase maps. (H) The main deformation mechanisms of CCA11 is phase transformation as shown in phase maps.

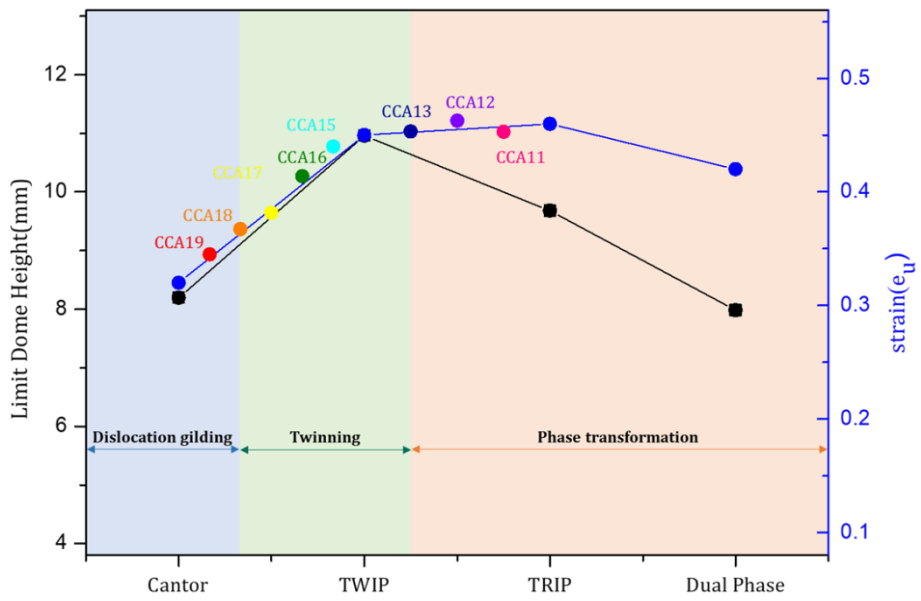


Figure 5.3. Comparison of uniform elongation between new CCAs systems and Cantor, TWIP, TRIP, and TaDP CCAs.

Bibliography

- [1] K.G. Pradeep, C.C. Tasan, M. Yao, Y. Deng, H. Springer, D. Raabe, Non-equiatomic high entropy alloys: Approach towards rapid alloy screening and property-oriented design, *Materials Science and Engineering: A* 648 (2015) 183-192.
- [2] J.W. Yeh, S.K. Chen, S.J. Lin, J.Y. Gan, T.S. Chin, T.T. Shun, C.H. Tsau, S.Y. Chang, Nanostructured high-entropy alloys with multiple principal elements: novel alloy design concepts and outcomes, *Advanced Engineering Materials* 6(5) (2004) 299-303.
- [3] C.-Y. Hsu, J.-W. Yeh, S.-K. Chen, T.-T. Shun, Wear resistance and high-temperature compression strength of Fcc CuCoNiCrAl 0.5 Fe alloy with boron addition, *Metallurgical and Materials Transactions A* 35(5) (2004) 1465-1469.
- [4] B. Gludovatz, A. Hohenwarter, K.V. Thurston, H. Bei, Z. Wu, E.P. George, R.O. Ritchie, Exceptional damage-tolerance of a medium-entropy alloy CrCoNi at cryogenic temperatures, *Nature communications* 7 (2016) 10602.
- [5] D.B. Miracle, O.N. Senkov, A critical review of high entropy alloys and related concepts, *Acta Materialia* 122 (2017) 448-511.
- [6] B. Gludovatz, A. Hohenwarter, D. Catoor, E.H. Chang, E.P. George, R.O. Ritchie, A fracture-resistant high-entropy alloy for cryogenic applications, *Science* 345(6201) (2014) 1153-1158.
- [7] Y. Chen, T. Duval, U. Hung, J. Yeh, H. Shih, Microstructure and electrochemical properties of high entropy alloys—a comparison with type-304 stainless steel, *Corrosion science* 47(9) (2005) 2257-2279.
- [8] C.-Y. Hsu, C.-C. Juan, W.-R. Wang, T.-S. Sheu, J.-W. Yeh, S.-K. Chen, On the superior hot hardness and softening resistance of AlCoCr_xFeMo_{0.5}Ni high-entropy

- alloys, *Materials Science and Engineering: A* 528(10-11) (2011) 3581-3588.
- [9] O.N. Senkov, G. Wilks, J. Scott, D.B. Miracle, Mechanical properties of Nb₂₅Mo₂₅Ta₂₅W₂₅ and V₂₀Nb₂₀Mo₂₀Ta₂₀W₂₀ refractory high entropy alloys, *Intermetallics* 19(5) (2011) 698-706.
- [10] M.-H. Tsai, J.-W. Yeh, High-entropy alloys: a critical review, *Materials Research Letters* 2(3) (2014) 107-123.
- [11] W.-Y. Tang, J.-W. Yeh, Effect of aluminum content on plasma-nitrided Al x CoCrCuFeNi high-entropy alloys, *Metallurgical and materials transactions A* 40(6) (2009) 1479-1486.
- [12] J.-W. Yeh, S.-Y. Chang, Y.-D. Hong, S.-K. Chen, S.-J. Lin, Anomalous decrease in X-ray diffraction intensities of Cu–Ni–Al–Co–Cr–Fe–Si alloy systems with multi-principal elements, *Materials chemistry and physics* 103(1) (2007) 41-46.
- [13] S. Ranganathan, Alloyed pleasures: multimetallic cocktails, *Current science* 85(5) (2003) 1404-1406.
- [14] Y. Zhang, Y.J. Zhou, J.P. Lin, G.L. Chen, P.K. Liaw, Solid-solution phase formation rules for multi-component alloys, *Advanced Engineering Materials* 10(6) (2008) 534-538.
- [15] Y. Zhang, T.T. Zuo, Z. Tang, M.C. Gao, K.A. Dahmen, P.K. Liaw, Z.P. Lu, Microstructures and properties of high-entropy alloys, *Progress in Materials Science* 61 (2014) 1-93.
- [16] K.-Y. Tsai, M.-H. Tsai, J.-W. Yeh, Sluggish diffusion in Co–Cr–Fe–Mn–Ni high-entropy alloys, *Acta Materialia* 61(13) (2013) 4887-4897.
- [17] W.F. Hosford, R.M. Caddell, *Metal forming: mechanics and metallurgy*, Cambridge University Press 2011.

- [18] E. Atzema, Formability of auto components, Automotive Steels, Elsevier 2017, pp. 47-93.
- [19] K. Chung, K. Ahn, D.-H. Yoo, K.-H. Chung, M.-H. Seo, S.-H. Park, Formability of TWIP (twinning induced plasticity) automotive sheets, International Journal of Plasticity 27(1) (2011) 52-81.
- [20] J.-H. Pi, Y. Pan, L. Zhang, H. Zhang, Microstructure and property of AlTiCrFeNiCu high-entropy alloy, Journal of Alloys and Compounds 509(18) (2011) 5641-5645.
- [21] B. Schuh, F. Mendez-Martin, B. Völker, E.P. George, H. Clemens, R. Pippan, A. Hohenwarter, Mechanical properties, microstructure and thermal stability of a nanocrystalline CoCrFeMnNi high-entropy alloy after severe plastic deformation, Acta Materialia 96 (2015) 258-268.
- [22] C. Ten Broek, H. Singh, M. Hillebrecht, Lightweight design for the future steel vehicle, Auto Tech Review 1(11) (2012) 24-30.
- [23] M. Takahashi, Development of high strength steels for automobiles, Shinnittetsu Giho (2003) 2-6.
- [24] S.P. Keeler, Plastic instability and fracture in sheets stretched over rigid punches, Massachusetts Institute of Technology, 1961.
- [25] G.M. Goodwin, Application of strain analysis to sheet metal forming problems in the press shop, SAE Transactions (1968) 380-387.
- [26] K. Nakazima, T. Kikuma, K. Hasuka, Study on the formability of steel sheets, YAWATA TECH REP, SEPT. 1968,--264--, 8517-8530 (1968).
- [27] K. Chung, M.-G. Lee, Basics of Continuum Plasticity, Springer 2018.
- [28] S. Panich, F. Barlat, V. Uthaisangasuk, S. Suranuntchai, S. Jiratheeranat,

Experimental and theoretical formability analysis using strain and stress based forming limit diagram for advanced high strength steels, *Materials & Design* 51 (2013) 756-766.

[29] J. Schey, Surface preparation for the LDH test, *Journal of Materials Shaping Technology* 6(2) (1988) 103-111.

[30] V. Karthik, R. Comstock Jr, D. Hershberger, R. Wagoner, Variability of sheet formability and formability testing, *Journal of materials processing technology* 121(2-3) (2002) 350-362.

[31] Y. Bao, T. Wierzbicki, On fracture locus in the equivalent strain and stress triaxiality space, *International Journal of Mechanical Sciences* 46(1) (2004) 81-98.

[32] P.W. Bridgman, *Studies in large plastic flow and fracture*, McGraw-Hill New York 1952.

[33] Y. Bao, Dependence of ductile crack formation in tensile tests on stress triaxiality, stress and strain ratios, *Engineering fracture mechanics* 72(4) (2005) 505-522.

[34] O. Grässel, L. Krüger, G. Frommeyer, L. Meyer, High strength Fe–Mn–(Al, Si) TRIP/TWIP steels development—properties—application, *International Journal of plasticity* 16(10-11) (2000) 1391-1409.

[35] C. Herrera, D. Ponge, D. Raabe, Design of a novel Mn-based 1 GPa duplex stainless TRIP steel with 60% ductility by a reduction of austenite stability, *Acta Materialia* 59(11) (2011) 4653-4664.

[36] S. Wei, J. Kim, C.C. Tasan, Boundary micro-cracking in metastable Fe45Mn35Co10Cr10 high-entropy alloys, *Acta Materialia* 168 (2019) 76-86.

[37] G.B. Olson, M. Cohen, A general mechanism of martensitic nucleation: Part I.

General concepts and the FCC→ HCP transformation, *Metallurgical Transactions A* 7(12) (1976) 1897-1904.

[38] E.S. Park, H.S. Oh, K. SangJun, K. Yoon, C.W. Ryu, High entropy alloy having TWIP/TRIP property and manufacturing method for the same, Google Patents, 2019.

[39] H.W. Swift, Plastic instability under plane stress, *Journal of the Mechanics and Physics of Solids* 1(1) (1952) 1-18.

[40] E. Voce, The relationship between stress and strain for homogeneous deformation, *Journal of the Institute of Metals* 74 (1948) 537-562.

[41] R. Hill, A theory of the yielding and plastic flow of anisotropic metals, *Proceedings of the Royal Society of London. Series A. Mathematical and Physical Sciences* 193(1033) (1948) 281-297.

[42] F. Barlat, J. Brem, J.W. Yoon, K. Chung, R. Dick, D. Lege, F. Pourboghrat, S.-H. Choi, E. Chu, Plane stress yield function for aluminum alloy sheets—part 1: theory, *International Journal of Plasticity* 19(9) (2003) 1297-1319.

[43] J.-W. Yoon, F. Barlat, R.E. Dick, K. Chung, T.J. Kang, Plane stress yield function for aluminum alloy sheets—part II: FE formulation and its implementation, *International Journal of Plasticity* 20(3) (2004) 495-522.

[44] F. Djavanroodi, A. Derogar, Experimental and numerical evaluation of forming limit diagram for Ti6Al4V titanium and Al6061-T6 aluminum alloys sheets, *Materials & Design* 31(10) (2010) 4866-4875.

[45] T. Naka, G. Torikai, R. Hino, F. Yoshida, The effects of temperature and forming speed on the forming limit diagram for type 5083 aluminum–magnesium alloy sheet, *Journal of Materials Processing Technology* 113(1-3) (2001) 648-653.

[46] B. De Cooman, O. Kwon, K.-G. Chin, State-of-the-knowledge on TWIP steel,

Materials Science and Technology 28(5) (2012) 513-527.

[47] K. Renard, H. Idrissi, D. Schryvers, P. Jacques, On the stress state dependence of the twinning rate and work hardening in twinning-induced plasticity steels, Scripta Materialia 66(12) (2012) 966-971.

[48] D. Ludwigson, J.A. Berger, Plastic behaviour of metastable austenitic stainless steels, J Iron Steel Inst 207(1) (1969) 63-69.

초 록

변형 기구에 따른 콤플렉스 고용 합금의 성형성 평가

예정원

서울대학교 공과대학

재료공학부

콤플렉스 고용 합금(CCAs)은 높은 응력과 고온 환경과 같은 극한 환경에서 기존의 상용 합금 대비 높은 강도와 연신을 포함하여 우수한 기계적 특성을 갖기 때문에 새로운 구조 재료로 각광받고 있다. 그런데 재료가 구조재료로서 사용되기 위해서는 재료의 소성 변형과 밀접한 관계가 있는 성형성 평가가 필요하다. 따라서 본 연구에서는 FCC CCAs의 변형 기구에 따른 성형성 평가를 진행하고자 하였다. 이를 위해 열역학적 계산을 통해 재료의 적층결함에너지를 제어하여 dislocation gliding(slip), twinning induced plasticity(TWIP), 그리고 transformation induced plasticity(TRIP, TaDP)와 같이 서로 다른 변형 기구를 갖는 콤플렉스 고용 합금을 제조하였다. 위 재료에 대한 성형성 평가 방법으로는 시뮬레이션을 통한 forming limit diagram(FLD) 작도와 실험을 통한 재료의 limit dome height(LDH) 실험을 진행하였다. Marciniak-Kuczinsky(M-K) model을 사용하여 FCC CCAs의 FLD를 작도하였고, 결과적으로 CCAs의 성형능이 일축 인장 실험에서의 uniform elongation과 동일한 경향성을 갖는 것을 확인하였다.

추가적으로 LDH 실험을 통해 재료의 LDH 값을 비교를 진행하였고, 이를 통해 상변화 기반 변형 기구를 갖는 TRIP, TaDP CCAs의 경우 일축 인장 상태에서의 uniform elongation과 다르게 성형능이 감소하는 것을 알 수 있었다. 이러한 현상을 이해하기 위해 판상 성형에서 주된 응력 상태인 평면 응력 상태와 일축 인장 실험에서 주된 응력 상태인 일축 응력 상태의 미세구조 분석을 진행하고자 하였다. 이를 위해 일반적으로 변형시 일축 변형 상태를 갖는다고 알려진 central hole test와 평면 변형 상태를 갖는다고 알려진 notched test를 수행하였다. 변형 상태에 따른 변형 거동 차이를 이해하기 위해, TWIP CCA에서는 electron channeling contrast image(ECCI) 분석을 통한 twinning thickness 비교, TRIP, TaDP CCAs에서는 electron backscatter diffraction(EBSD) 분석을 통한 phase fraction 비교를 진행하였다. 이를 통해 dislocation gliding 혹은 twinning 변형 기구를 갖는 재료의 경우 응력 상태 따라 성형능에 변화가 없으나, 상변화 기반 변형 기구를 갖는 재료의 경우 일축 응력 상태에서 이축 응력 상태로 갈수록 상변화 거동이 저하되어 성형능이 감소하는 것을 확인 하였다. 위 결과를 바탕으로 본 논문은 성형성이 최적화된 콤플렉스 고용 합금 설계의 방법을 제공할 수 있었다.

핵심어: 콤플렉스 고용 합금, 변형 기구, forming limit diagram (FLD), limit dome height test (LDH), 응력 상태 분석

학번: 2018-25610